Hindawi
Structural Control and Health Monitoring
Volume 2023, Article ID 8940008, 30 pages
https://doi.org/10.1155/2023/8940008

Review Article

Nondestructive Testing and Health Monitoring Techniques for Structural Effective Prestress

Junfeng Jia[1], **Longguan Zhang**[1], **Jinping Ou**[1,2] **and Xize Chen**[1]

[1]*State Key Laboratory of Bridge Engineering Safety and Resilience, Beijing University of Technology, Beijing 100124, China*
[2]*School of Civil Engineering, Harbin Institute of Technology, Shenzhen 518055, China*

Correspondence should be addressed to Junfeng Jia; jiajunfeng@bjut.edu.cn

Received 6 December 2022; Revised 8 September 2023; Accepted 14 September 2023; Published 28 September 2023

Academic Editor: Ka-Veng Yuen

Prestressed structures are widely employed in bridges and large-span spatial structures, and the accurate evaluation of prestress state is of great importance for structural maintenance. This paper reviews the nondestructive testing (NDT) and health monitoring techniques for structural effective prestress. Specifically, the fiber Bragg grating (FBG) sensor-based, magnetic-elastic (ME) sensor-based, dynamic response-based, ultrasonic guided wave (UGW)-based, electromechanical impedance (EMI)-based, and electrical resistance-based methods are reviewed in this paper. Firstly, the principle, application range, and measuring accuracy of each technique are introduced and analyzed, and the benefits and limitations of each technique are summarized: The FBG sensor and ME sensor take on high measuring accuracy and have been applied in practical engineering, but they are required to be preinstalled during structural construction; the dynamic response-based method is greatly effective in cable force assessment but not suitable for prestress evaluation of prestressed concrete (PSC) structures; the UGW-based, EMI-based, and electrical resistance-based methods have shown favorable potential for prestress assessment in laboratory experiments, but their feasibility and accuracy in practical engineering need to be verified. Secondly, the challenges and discussion of each method are discussed in the following four aspects: measuring range, reliability of measuring results, stability and durability considering long-term monitoring, and cost-efficiency. Finally, a decision tree is proposed to choose the most appropriate prestress evaluation method in a specific application scenario.

1. Introduction

To increase structural bearing capacity and service performance, prestress is commonly applied to a certain part of the structure, and typical prestressed structures include cable-supported bridges [1, 2], PSC structures [3, 4], and prestressed anchor-reinforced slopes [5]. In terms of the abovementioned structures, the value of effective prestress during service plays a crucial role in their security state. However, the prestress losses due to concrete shrinkage and creep [6, 7], duct friction [8], relaxation of steel strands [9], corrosion [10], and other external effects [11] are unavoidable. Once the effective prestress is reduced to a certain threshold, the structural performance can be significantly degraded and may even lead to structural damage [12, 13]. The current codes, such as JTG 3362 [14], ACI 318-08 [15], and AASHTO-LRFD [16], estimate prestress loss based on empirical formulas only, and there are large deviations between estimated results and the actual prestress loss [17–19]. In addition, in prestress evaluation using the finite element model, the uncertainties in environmental conditions, boundary conditions, material parameters, and structural dimensions can also cause difficulties in accurate assessment of effective prestress [20, 21]. Therefore, to provide timely warning of structural degradation due to prestress loss, it is necessary to adopt appropriate approaches to measure and monitor structural effective prestress.

NDT is a technique for detecting and identifying structural internal defects without causing damage to the object being tested [22, 23]. The current NDT approaches commonly utilized in engineering include ultrasonic testing

[24, 25], radiographic testing [26, 27], magnetic particle testing [28], penetrant testing [29, 30], and eddy current testing [31, 32]. In terms of the abovementioned techniques, damage location and quantification are accomplished based on changes in the acoustic, optical, electrical, and magnetic properties caused by internal defects, and some of the approaches require direct contact between the test devices and the object being tested. However, the prestressed steel strands are usually installed inside the grout and concrete, and the steel cables are wrapped with HDPE sheaths, which make it difficult to apply certain contact testing devices to the above structures. However, there are still some NDT approaches that have shown great potential for prestress estimation, such as UGW-based [33, 34] and electrical resistance-based [35] methods.

Structural health monitoring (SHM) is a technique that uses sensors installed inside or on the surface of the structure to obtain the structural response in real time and then evaluate the global and local security state [36, 37]. As for prestress monitoring, the most direct and effective way is to install sensors, such as load cells and strain gauges, during construction state [38, 39], but such sensors are easily damaged and with low measuring accuracy. Embedded FBG sensors [40] and ME sensors [41], which have been rapidly developed in recent years, are considered effective means to monitor prestress loss due to their high accuracy and durability. Furthermore, using lead zirconate titanate (PZT) sensors [42], which are able to monitor the variation of EMI due to prestress loss, is also a viable approach. Accelerometers, as the most commonly used sensor type in SHM systems, can also play a role in structural prestress monitoring [43], whose monitoring principle is to obtain dynamic response and then back-calculate the prestress state.

This paper aims to review the NDT and SHM techniques for structural effective prestress. Specifically, the FBG sensor-based, ME sensor-based, dynamic response-based, UGW-based, EMI-based, and electrical resistance-based methods are reviewed. Firstly, the principle, application range, and measuring accuracy of each technique are introduced and analyzed, and the benefits and limitations of each technique are summarized; secondly, the challenges and discussions of each method are discussed in the following four aspects: measuring range, reliability of measuring results, stability and durability considering long-term monitoring, and cost-efficiency; finally, a decision tree is proposed to choose the most appropriate prestress evaluation method in a specific application scenario.

2. Review of Various Prestress Evaluation Methods

2.1. FBG Sensor-Based Method. The FBG sensor is widely employed in SHM systems for various structures due to its high interference immunity, small size, low transmission loss, and wide measuring range, and the diagram of FBG sensor is shown in Figure 1 [44]. According to grating theory, when the light wavelength spectrum is launched in the FBG sensor, the wavelength corresponding to the conditions of the Bragg gratings is reflected, while the other wavelengths pass through. The peak of reflected wavelength can be shifted by $\Delta\lambda$ when the grating is subjected to external physical fields (e.g., temperature and stress). Thus, the changes in stress and temperature can be determined by $\Delta\lambda$.

The FBG sensor used for structural prestress monitoring has been deeply investigated and realized engineering applications, as shown in Table 1. The FBG needs to be carefully encapsulated due to its brittle quality and weak shear resistance, especially when the FBG sensor is embedded in concrete, the sensor can be damaged if it is not properly encapsulated [59]. According to Table 1, there are 2 encapsulating approaches for FBG sensors: one is surface-bonded, i.e., the FBG sensor is fixed to steel surface with adhesive [45, 52, 56], as shown in Figures 2(a) and 2(b). Although it is easy to install in this way, the sensor and its connecting wire are susceptible to be broken by the friction between steel strand and duct. The other approach is to embed FBG sensors in the core wire of the strand, which enables the steel strand to realize the integrated function of bearing and sensing and is therefore known as smart strand (or self-sensing strand), and similar to this is smart cable [47]. The current techniques for manufacturing smart steel strands mainly include fusing FBG sensor and fiber reinforced polymer (FRP) material into a whole by heating cure processing [46–48, 50, 51, 53, 54, 57, 58] and embedding FBG sensor into a hollow steel tube and injecting epoxy glue into the tube to achieve a reliable bond between the FBG and the tube [44, 49, 55]. In addition, Zhu et al. [40] proposed a new method that encapsulating the FBG sensor in a longitudinal groove of the core wire, which allows FBG and core wire to be deformed synchronously.

In addition to the embedding and encapsulating method, the measuring accuracy, performance in service, and measuring range are also the main research contents of FBG sensors. In terms of measuring accuracy, several scholars have evaluated the effective prestress of PSC girders and steel cables using embedded FBG sensors, and the results were compared with conventional sensors such as strain gauges and load cells. The FBG sensors show fairly high measuring accuracy [46, 48–52, 58], and the specific measuring errors can be seen in Table 1.

The performance in service refers to the bonding performance and codeformation ability between FBG sensor and the object to be measured. Li et al. [48] conducted repeated loading and unloading experiments on a smart suspender with embedded GFRP-OFBG composite bars in the laboratory, and no relative sliding occurred between GFRP-OFBG composite bars and other steel wires throughout the experiments. He et al. [50] observed that the embedded FRP-OF-FBG composite bars maintained consistent deformation with the cable even under high-stress state. However, Dan et al. [57] found relative slip between the internal smart composite bar and other steel wires due to nonuniform longitudinal connection. In this regard, they suggested increasing the contact and engagement forces between the steel wires and smart bar during production.

It is well known that prestressed steel strands and high-strength steel wires are subjects to fatigue loading during service, leading to a wide range of changes in stress and

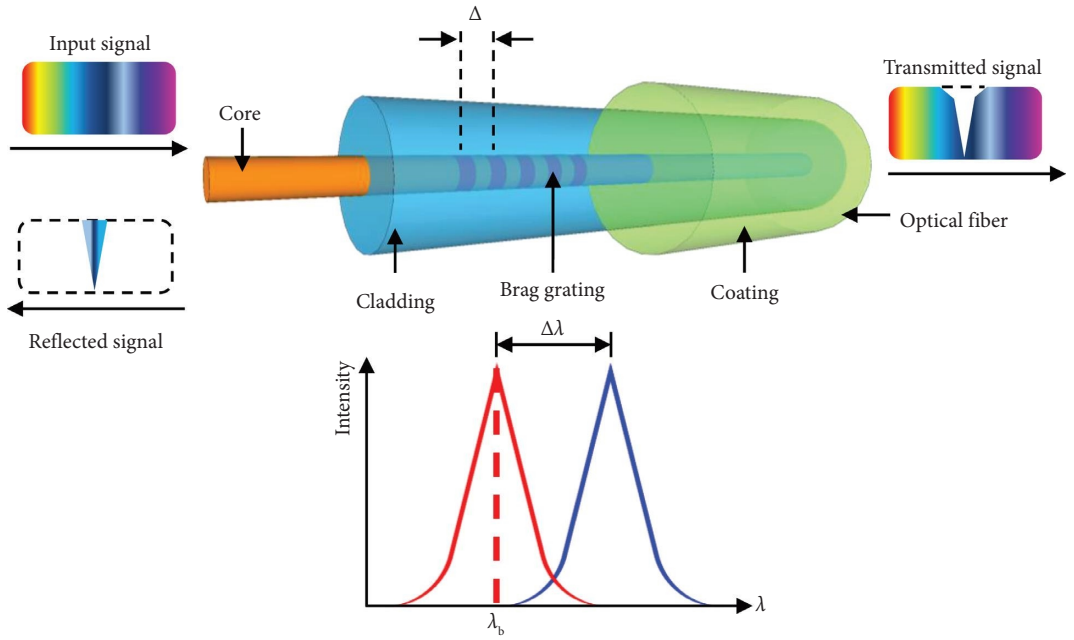

Figure 1: Diagram of FBG sensor.

strain, which raises higher requirements of measuring range for FBG sensors. Li et al. [47] attached GFRP-OFBG smart bars with different diameters (φ3.5 mm, φ5 mm, and φ7 mm) to the surface of φ15.2 mm steel strand by using AB glue and conducted tensile tests on them. Results show that the ultimate strain of the smart bar increases with diameter, and the ultimate strain of φ7 mm smart bar is about 8000 $\mu\varepsilon$, indicating that the φ7 mm smart bar can monitor 75% of the ultimate strain for steel strand with a diameter of 15.2 mm and an ultimate strength of 1860 MPa. Relevant Chinese codes [60, 61] stipulate that the design load of bridge cables should be less than 40% of the ultimate load; therefore, the smart bar with a diameter of 7 mm can meet the strain monitoring requirements of bridge cables. However, Jiao et al. [58] pointed out that the above GFRP-OFBG smart bars could not monitor the fracture strain of steel strands; hence, a coaxial cable Fabry–Perot interferometer (CCFPI) sensor was encapsulated into the GFRP material to form a GFRP-CCFPI smart bar. The test results show the smart bars realize the monitoring of fracture strain with a maximum measured strain of 16000 $\mu\varepsilon$. Kim et al. [55] proposed a technique to coat the surface of the FBG sensor with polyimide to improve its maximum measured strain, and results indicate that the maximum strain measured by the FBG sensor using the proposed technique is 1.73 times of the yield strain of steel strand, while that of the conventional FBG sensor was only 0.65 times of the yield strain of steel strand.

In summary, in terms of structural prestress monitoring based on embedded FBG sensors, the current research mainly focuses on the embedding and encapsulating process, measuring accuracy, performance in service, and measuring range. The embedded FBG sensor is capable of directly and effectively measuring changes in structural prestress with high accuracy and has been implemented for engineering applications in several fields. However, the FBG sensor must be preinstalled during construction, and in other words, it is not applicable to in-service structures without preinstalled FBG sensors.

2.2. ME Sensor-Based Method. When a ferromagnetic material is magnetized by an external magnetic field, its volume and length will be changed, which is called magnetostrictive effect [62]. Conversely, when a ferromagnetic material is deformed by an external force, its magnetism will also be changed, which is called inverse magnetostrictive effect, also known as the magnetoelastic (ME) effect [63]. The principle of structural prestress evaluation based on ME effect can be expressed as follows.

When the material is subjected to axial tension force F, in the elastic region, the axial strain ε can be expressed as

$$\varepsilon = \frac{\sigma}{E} = \frac{F}{EA}, \tag{1}$$

where F refers to the axial tensile force and E and A refer to the elastic modulus and cross-sectional area of the material, respectively. According to the Joule effect, the axial strain of the material can also be expressed as [64]

$$\varepsilon = \frac{\Delta l}{l} = \frac{3\lambda_S M_S}{2K_u} \Delta M \sin^2\theta_0 \cos\theta_0, \tag{2}$$

Table 1: Research studies on structural prestress monitoring based on FBG sensors.

Publication year	Researchers	Measuring object	Laboratory or field	Encapsulating and embedding method	Measuring error	Note
1996	Nellen et al. [45]	Prestressed carbon fiber cable	Laboratory	FBG sensor was fixed on the strand surface using glue and Teflon tape	—	—
2009	Zhou et al. [46]	PSC beam	Laboratory	FBG sensor was embedded in an FRP bar	Within 5%	Smart steel strand
2011	Li et al. [47]	Stay cable	Laboratory	FBG sensor was embedded in a GFRP bar	With a maximum error of 11.86%	Smart stay cable
2012	Li et al. [48]	Arch bridge suspender	Both	FBG sensor was embedded in a GFRP bar	—	Smart suspender
2012	Kim et al. [49]	PSC beam	Both	FBG sensor was encapsulated by epoxy resin and steel tube	Within 5%	Smart steel strand
2013	He et al. [50]	Bridge cable	Laboratory	FBG sensor was embedded in a FRP bar	Within 5%	Smart cable
2014	Lan et al. [51]	PSC beam	Laboratory	FBG sensor was embedded in a FRP bar	Within 5%	Smart steel strand
2014	Li and Zhou [52]	Bridge cable	Laboratory	Using adhesive to join FBG sensor and steel wire	Within 4.5%	—
2015	Kim et al. [53]	Steel strand	Laboratory	FBG sensor was embedded in a carbon core wire	—	Smart steel strand
2016	Kim et al. [44]	Pretensioned UHPC deck	Both	FBG sensor was encapsulated by epoxy resin and steel tube	—	Smart steel strand
2017	Huynh and Kim [54]	PSC girder	Laboratory	FBG sensor was embedded in a carbon core wire	—	Smart tendon
2017	Kim et al. [55]	Steel strand	Laboratory	FBG sensor was encapsulated by epoxy resin and steel tube	—	Smart steel strand
2018	Zheng et al. [56]	Steel wire for bridge cable	Laboratory	Using structural adhesive to join FBG sensor and steel wire	—	—
2018	Dan et al. [57]	Steel strand	Laboratory	FBG sensor was embedded in a carbon fiber bar	—	Smart tendon
2020	Jiao et al. [58]	Steel strand	Laboratory	FBG sensor was embedded in a FRP bar	Within 7%	Smart steel strand
2021	Zhu et al. [40]	PSC beam	Laboratory	FBG sensor was embedded in the groove of the center wire		Self-sensing steel strand

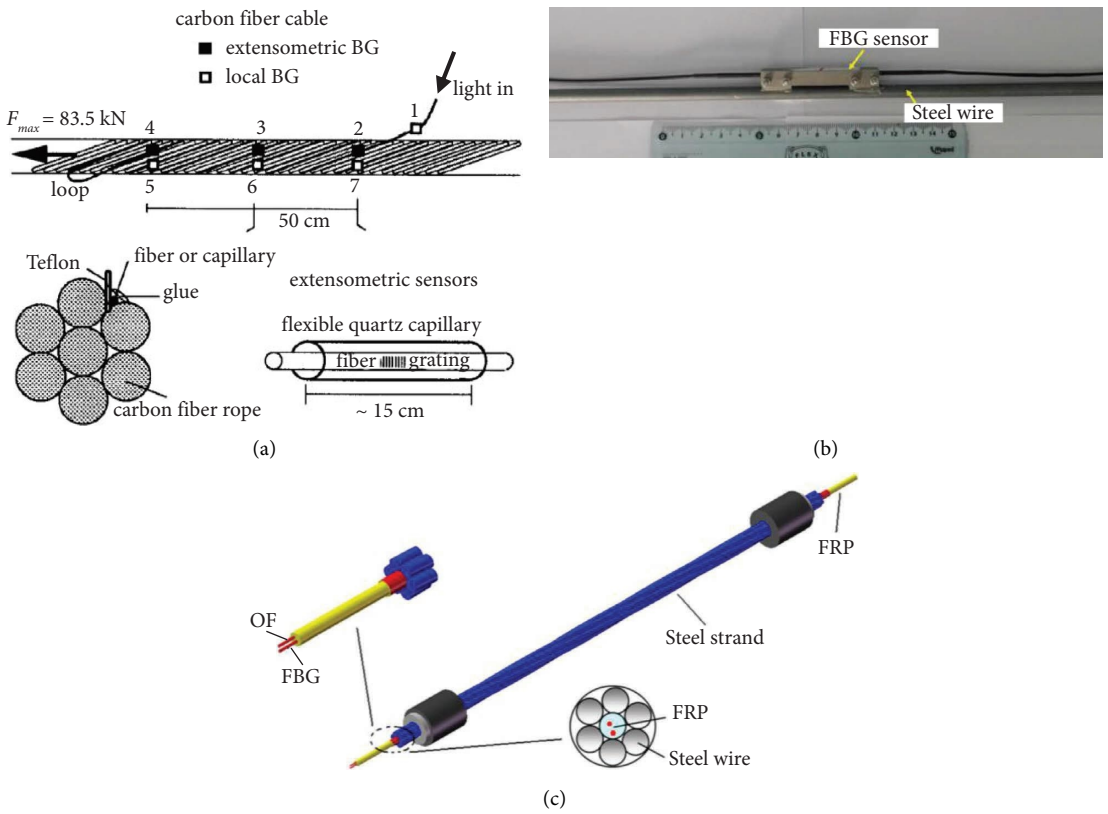

FIGURE 2: Encapsulations of FBG sensors. (a) FBG sensor was fixed on the strand surface using glue and Teflon tape [45]. (b) The adhesive-bonded FBGs seats-steel wires structure [56]. (c) FBG sensor was embedded into the FRP bar in a smart steel strand [51].

where λ_s refers to the constant for axial deformation, M_s refers to the saturation magnetization, K_u refers to the magnetic anisotropy constant of a single axis, θ_0 refers to the angle between the magnetic field and the easy magnetization axis, and ΔM refers to the change in magnetization under external force. ΔM can be expressed as

$$\Delta M = (\mu - \mu_0)H = \Delta\mu \cdot H, \tag{3}$$

where H refers to the magnetic field intensity, μ refers to the permeability, μ_0 refers to the air permeability, and $\Delta\mu$ refers to the change in permeability under external force. According to equations (1)–(3),

$$F = \mathrm{EA}\frac{3\lambda_S M_S}{2K_u}\Delta\mu H \sin^2\theta_0 \cos\theta_0. \tag{4}$$

Equation (4) shows that there is a proportional relationship between F and $\Delta\mu$. The value of F can be calculated so long as $\Delta\mu$ can be accurately measured.

Based on the above theory, several scholars have developed ME sensors that can measure the change in permeability, and structural prestress was also obtained using ME sensors, as shown in Table 2. In terms of the ME sensor-based method, current research focuses on the development of sensors with new types and the effect of temperature on the service performance of the ME sensor.

In the research of developing new type of sensors, conventional ME sensor mainly consists of a primary coil (as the excitation coil), a secondary coil (as the induction coil), and an object to be measured (steel cable and steel strand), as shown in Figure 3(a) [65]. Its operating principle can be expressed as follows: when a pulse or alternating current is passed through the excitation coil, an excitation magnetic field is generated and the measured object is magnetized. Then, the magnetized object generates an induced magnetic field along its longitudinal direction, after which the induction coil generates an induced voltage. The value of induced voltage depends on magnetic permeability of the measured object. The abovementioned double-coil type sensor is also the most widely used one of the ME sensors [65, 66, 69, 73, 75–77, 80]. However, this type of sensor shows some shortcomings, such as complex design, difficult installation, low signal-to-noise ratio, and slow response [41, 71]. To solve these shortcomings, numerous scholars have researched developing ME sensors with new types. Zhang et al. [68, 71, 74] developed an elastomagnetoelectric (EME) sensor based on the elastomagnetic effect and magnetoelectric effect, as shown in Figure 3(b). The sensor replaces the secondary coil (induction coil) with a smart magnetoelectric sensing element, numerical simulations and laboratory experiments results demonstrate that the magnetoelectric sensing element owns a faster response speed, and its sensitivity is more than 10 times that of secondary

Table 2: Research studies on structural prestress monitoring based on ME sensors.

Publication year	Researchers	Measuring object	Laboratory or field	Measuring error
2005	Sumitro et al. [65]	PSC tendon, stay cable	Both	Within 10%
2008	Tang et al. [66]	Steel cable	Laboratory	—
2013	Joh et al. [67]	Prestressed tendon	Laboratory	—
2014	Zhang et al. [68]	Steel cable	Laboratory	—
2014	Tang et al. [69]	Steel cable	Laboratory	—
2016	Cho et al. [70]	PSC steel strands	Laboratory	—
2016	Duan et al. [71]	Stay cable	Both	Within 2%
2017	Xiu et al. [72]	Steel cable	Laboratory	—
2018	Ren et al. [73]	Steel cable	Both	
2018	Zhang et al. [74]	Steel cable	Laboratory	—
2018	Chen and Zhang [75]	PSC tendon	Laboratory	—
2018	Liu et al. [76]	Steel strand	Laboratory	0–7.7%
2018	Feng et al. [77]	Stay cable	Field	—
2018	Guo et al. [78]	PSC tendon	Laboratory	—
2019	Zhang et al. [64]	Steel cable	Laboratory	—
2020	Kim and Park [79]	PSC tendon	Laboratory	—
2021	Liu et al. [80]	Steel wire rope	Laboratory	Within 5%
2021	Zhang et al. [41]	Steel strand	Laboratory	Within 10%
2021	Zhang et al. [81]	Steel strand	Laboratory	12.5%, 11.9%, and 9.5%

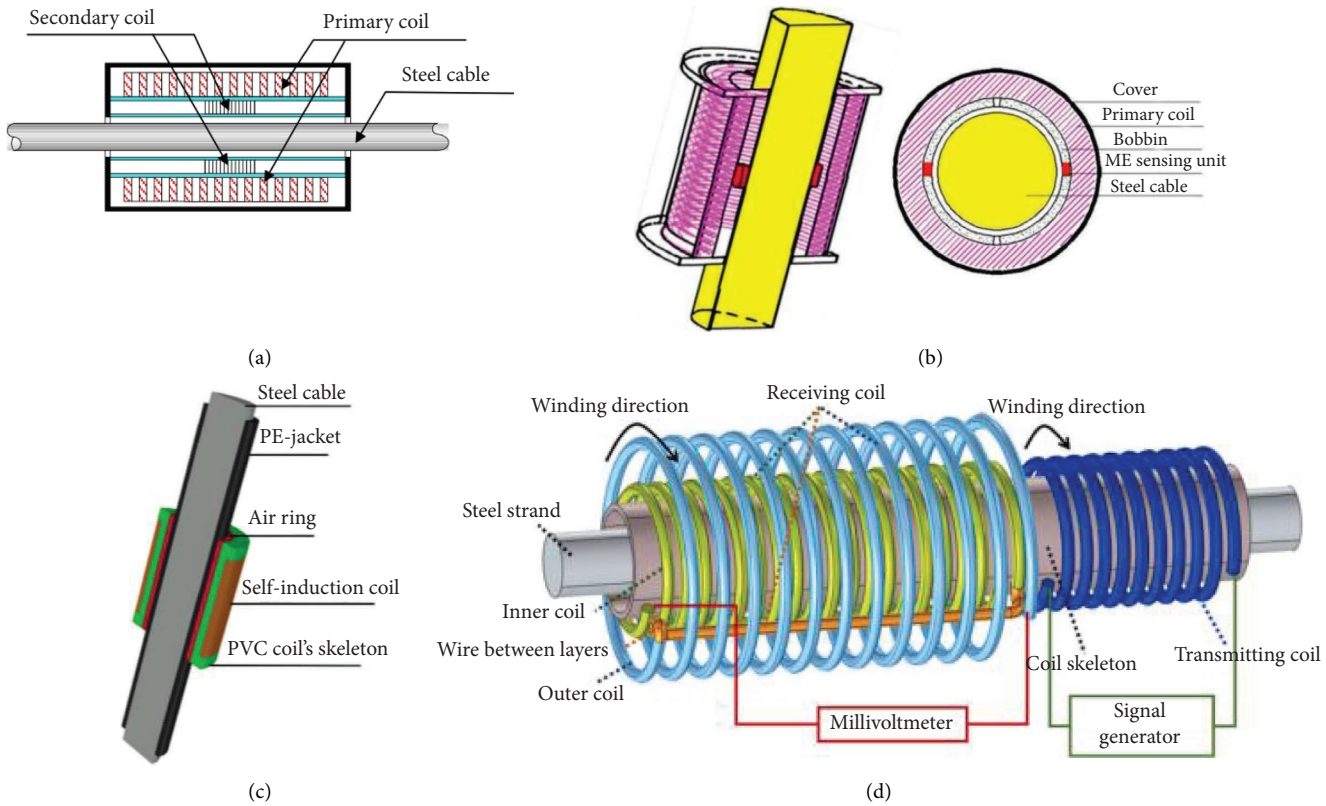

Figure 3: Diagram of several types of ME sensors. (a) Traditional ME sensor with dual coils [65]. (b) Smart elastomagnetoelectric (EME) sensor [68]. (c) ME sensor with a self-induction coil [64]. (d) Resonance-enhanced magnetoelastic (REME) sensor [81].

coil. Based on self-induction phenomenon, Zhang et al. [41, 64] simplified the conventional primary and secondary coils into a single self-induction coil, as shown in Figure 3(c). The feasibility of this sensor in tension force measuring for steel cable was verified by numerical simulations and laboratory experiments. Results indicate that the self-induction ME sensor has merits of high sensitivity, fast response, and ease of installation. According to the resonance theory, Zhang et al. [81] developed a resonance-enhanced magnetoelastic (REME) sensor with low power supply and good dynamic response, as shown in Figure 3(d). The basic principle is to adjust the excitation frequency of the

excitation coil to the resonance frequency of the induction coil, and thus, the magnetic coupling resonance is generated. Experimental results show that the introduction of resonance theory effectively improves the measuring sensitivity.

As mentioned above, the tension force of prestressed structures can be determined by the change in permeability, $\Delta\mu$. However, $\Delta\mu$ is not only governed by prestress but also by variation in temperature. In addition, the change in permeability due to temperature rising and dropping may vary considerably, making the use of temperature compensation curves for temperature error compensation ineffective [66]. The temperature variation of ME sensor is mainly influenced by the environmental temperature and the thermal effect of the coil, while the use of pulsed current excitation [65] can reduce the thermal effect to a certain extent. Moreover, several new approaches for temperature compensation have been investigated. Tang et al. [66] proposed an ME sensor with a different single bypass excitation structure; in addition to the working magnetic loop, a reference loop is also set in this sensor. The strand in reference loop is of the same material as the strand to be measured but is not involved in prestressing. Therefore, the output $\Delta\mu$ from reference loop is only caused by temperature variation, which is utilized as temperature compensation. Feng et al. [77] extracted ME characteristic parameters that are sensitive to changes in tension force but not in temperature, and a frequency domain parameter, i.e., the summation of spectra amplitudes, in particular, frequency band (S_{fre}), was introduced. Field test results show that S_{fre} in a specific frequency range is almost independent of temperature variations and reflects changes in cable force. In recent years, machine learning has shown unique advantages in dealing with structural nonlinear problems, Zhang et al. [74] developed an improved BP neural network to compensate for the nonlinear errors caused by temperature variations, and the measuring cable force after temperature compensation is within ±0.9%. The BP neural network-based temperature compensation algorithm exhibits good reliability, effectiveness, and robustness.

In summary, the ME sensor-based method effectively monitors structural prestress state with high measuring accuracy. Improved ME sensors significantly increase the response speed and measuring sensitivity. Changes in ME sensor temperature can also lead to changes in permeability, and appropriate temperature compensation approaches can be utilized to reduce the effects of temperature and improve measuring accuracy. However, similar to FBG sensors, ME sensors need to be preinstalled during structural construction phase, and therefore, such technique is not suitable for prestress monitoring of in-service structures without ME sensors installed.

2.3. Dynamic Response-Based Method. Once the structural damage occurs globally or locally, its natural properties (e.g. stiffness, damping, etc.) may be changed, leading to a change in its dynamic response. Therefore, structural damage identification and location can be realized through the monitoring of dynamic response (e.g., displacement, velocity, acceleration, etc.) [82, 83]. For prestressed structures, the dynamic response also varies with prestress; hence, structural prestress state can be inversely calculated by monitoring its dynamic response [84].

2.3.1. Dynamic Response-Based Cable Force Estimation. In the aspect of cable force estimation, the measuring method and calculation theory have received a great deal of attention [85]. The main focus of this work is prestress monitoring approaches, and therefore, only one classical cable force calculation theory considering bending stiffness is introduced here [86]. Taking the stay cable as an example, the mechanical model of the stay cable with tension force is shown in Figure 4, where F refers to tension force, L refers to cable length, EI refers to bending stiffness, w refers to the mass of a unit length, and g refers to gravitational acceleration. The differential equation of motion for stay cable can be expressed as

$$\frac{\omega}{g}\frac{\partial^2 y}{\partial t^2} + \mathrm{EI}\frac{\partial^4 y}{\partial x^4} - F\frac{\partial^2 y}{\partial x^2} = 0. \tag{5}$$

If a simply supported boundary is used at both ends of the cable, the cable force F can be calculated from the nth-order natural frequency f_n:

$$F = \frac{4\omega L^2}{g}\left(\frac{f_n}{n}\right)^2 - \frac{\mathrm{EI}\pi^2}{L^2}n^2. \tag{6}$$

The natural frequency of cable can be obtained from the Fourier transform (FT) of its dynamic response time history. Therefore, the key to dynamic response-based cable force estimation is to accurately and efficiently acquire the natural frequency of cable from monitoring data. The feasibility and accuracy of this method have been verified through laboratory and field experiments by several scholars, as listed in Table 3.

In earlier studies, the main method for dynamic response monitoring was attaching accelerometers to cable surface to capture its vibration acceleration. However, there are some limitations to this method considering field application: the installation of accelerometers is cumbersome and dangerous; the accelerometers are difficult to install in the middle of the cable, but only at the bottom, which, considering that the bottom of the cable is usually equipped with vibration damping devices, causes the vibration signal captured to be insignificant. In recent years, there has been widespread concern about noncontact measurement-based cable dynamic response monitoring. Compared to accelerometer-based approaches, noncontact approaches avoid cumbersome sensor installation procedures and enable vibration monitoring for the whole cable [102]. The most common one in noncontact approaches is image-based cable force identification, whose basic principle is to capture vibration images using cameras and then extract the displacement information from the target points, and finally, the vibration displacement time history is obtained. Benefiting from the development of digital image correlation [96] and computer vision [108] techniques, the accuracy of the image-based

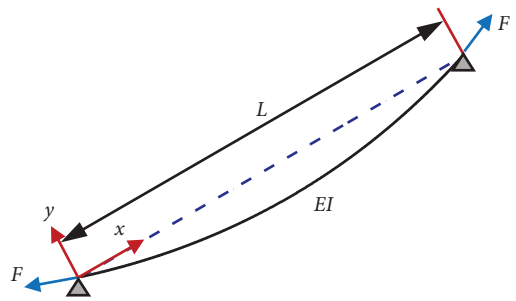

Figure 4: Mechanical model of the stay cable with tension force.

cable vibration monitoring approach has been improved continuously, which has reached and even exceeded that of the accelerometer-based approach [95]. In the image-based approach, the most commonly used device is a high-resolution camera at a fixed point [92, 93, 95–98, 101, 107–110]. For example, based on digital image processing and digital image correlation technique, Du et al. [96] achieved cable force identification with capturing single and multiple points images by the camera, and the relative deviation between the cable force measuring values based on the above two methods and the results based on the accelerometer is within 5%. In addition, Wang et al. [103] proposed a method for capturing vibration images using a smartphone. Tian et al. [102] and Zhang et al. [105] developed computer vision-based cable vibration measuring approaches using unmanned aerial vehicles. In both approaches, the camera devices are no longer limited to a fixed point, which allows for a higher degree of flexibility in field application. Furthermore, the acoustic radiation technique was first employed in cable vibration measuring [104], as shown in Figure 5. The forced cable vibration under the axial force F causes changes in near-field radiated acoustic pressure, and the radiated acoustic pressure signal is linearly proportional to the acceleration response of vibration source, indicating the vibration response can be determined from changes in near-field radiated acoustic pressure. The laboratory experiments showed the maximum average error in cable force between the proposed approach and accelerometers is less than 2%. Zhao et al. [94] presented a time-varying cable force assessment method for multiple cables based on microwave interferometric radar. The real-time displacement history of multicables was obtained using microwave interferometric radar, and then, the time-varying frequency identification of each cable was realized based on the blind source separation algorithm and Hilbert transform. The average relative error of the tested cables is less than 2%.

In summary, a high accuracy level is achieved in cable force estimation using the dynamic response-based method, and noncontact measuring approaches are becoming the mainstream due to their convenience.

2.3.2. Dynamic Response-Based Prestressing Force Estimation for PSC Structures. In PSC structures, structural stiffness can vary with its prestress state, leading to changes in natural frequency. It is therefore theoretically feasible to evaluate the effective prestress of PSC structure based on natural frequency. However, the relationship between natural frequency and prestress state for PSC structures has remained controversial. In terms of a homogeneous beam under external axial compression force, Saiidi et al. [111] proposed an equation for the correspondence between natural frequency f and external axial force F:

$$f_n^2 = -\left(\frac{n\pi}{L}\right)^2 \frac{F}{m} + \left(\frac{n\pi}{L}\right)^4 \frac{\mathrm{EI}}{m}, \tag{7}$$

where n refers to the modal number, L refers to the span length, F refers to the axial compression force, m refers to beam mass per unit length, and EI refers to bending stiffness. Equation (7) shows that an increase in the axial compression reduces the natural frequency, which is called "compression softening" effect. However, some scholars believe the application of prestress increases structural whole stiffness and therefore increases its natural frequency. Ho et al. [112] proposed the theory of considering the contribution of prestress as the equivalent bending stiffness of the prestressed strand. The mechanical model of the PSC girder is shown in Figure 6, and the prestress effect is represented by external force F. A small deformation δL is produced in the length direction when F is applied, the effective girder length is expressed as L_r, and the effective length of embedded prestress strand is expressed as L_s. The differential equation of motion for PSC girder can be expressed as follows:

$$\frac{\partial^2}{\partial x^2}\left(E_r I_r \frac{\partial^2 y}{\partial x^2}\right) + m_r \frac{\partial^2 y}{\partial t^2} = 0, \tag{8}$$

where $E_r I_r$ and m_r refer to cross-sectional effective bending stiffness and mass per unit length of the PSC girder, and the cross-sectional effective bending stiffness can be obtained by superimposing the bending stiffness of concrete and the equivalent bending stiffness of prestressed strand:

$$E_r I_r = E_c I_c + E_p I_p. \tag{9}$$

Similarly, the mass per unit length of the PSC girder is superimposed by the mass of the concrete and the mass of prestressed strand:

$$m_r = \rho_c A_c + \rho_p A_p, \tag{10}$$

where ρ_c, ρ_p and A_c, A_p refer to the density and cross-sectional area of concrete and prestressed strand, respectively. The modal property of strand subjected to prestressing force is equated to that of a girder with equivalent bending stiffness, and the equivalent bending stiffness of prestressed strand can be calculated as

$$E_s I_s = \left(\frac{L_s}{n\pi}\right)^2 F. \tag{11}$$

Combining the above equations, the nth-order natural frequency of the PSC girder is calculated as

Table 3: Research studies on cable force evaluation based on structural dynamic response.

Publication year	Researchers	Structural type	Acquisition method for vibration response	Laboratory or field	Testing error
2007	Kim and Park [87]	Stay cable	Accelerometer	Both	3%
2010	Cho et al. [88]	Stay cable	Accelerometer	Laboratory	Within 10%
2011	Choi and Park [89]	Stay cable	Accelerometer	Field	—
2014	Yu et al. [90]	Stay cable	Accelerometer	Both	Within 8%
2015	Zhao et al. [91]	Stay cable and suspender	Smartphone with built-in accelerometer	Both	Within 5%
2017	Bao et al. [85]	Cable	Accelerometer	Laboratory	Within 5%
2019	Rango et al. [92]	Stay cable	High-speed camera	Laboratory	Within 7%
2019	Yan et al. [93]	Stay cable	Video camera	Laboratory	Within 5%
2020	Zhao et al. [94]	Stay cable	Microwave interferometric radar	Field	Within 2%
2020	Kim et al. [95]	Hanger cable	Digital camera	Field	Within 2%
2020	Du et al. [96]	Stay cable	DSLR camera	Laboratory	Within 4%
2020	Yan et al. [97]	Hanger cable	Video camera	Both	Within 6%
2021	Chu et al. [98]	Stay cable	Camera	Laboratory	Within 5%
2021	Jeong et al. [99]	Stay cable	Accelerometer	Both	Within 6%
2021	Jana and Nagarajaiah [100]	Stay cable	Handheld camera	Field	Within 15%
2021	Jo et al. [101]	Stay cable	Digital camera	Field	—
2021	Tian et al. [102]	Hanger cable	Unmanned aerial vehicle	Both	Within 3%
2021	Wang et al. [103]	Stay cable	Smartphone	Field	Within 2%
2021	Yu et al. [104]	Cable	Acoustic radiation method	Laboratory	Within 2%
2022	Zhang et al. [105]	Stay cable	Drone	Both	—
2022	Jana et al. [106]	Stay cable	Accelerometer	Field	Within 3%
2022	Wangchuk et al. [107]	Stay cable	Video camera	Both	Within 8%
2022	Jana et al. [108]	Stay cable	Camera	Field	Within 8%
2023	Kim et al. [109]	Stay cable	Camera	Field	Within 3%
2023	Wang et al. [110]	Stay cable	Camera and unmanned aerial vehicle	Field	—

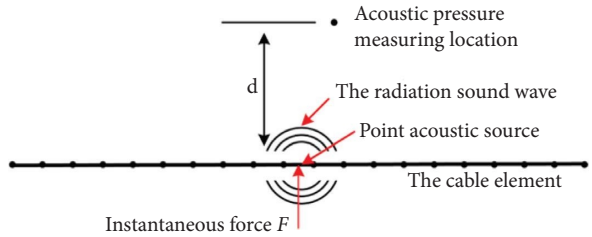

Figure 5: Diagram of vibration monitoring based on near-field radiated acoustic pressure signal [104].

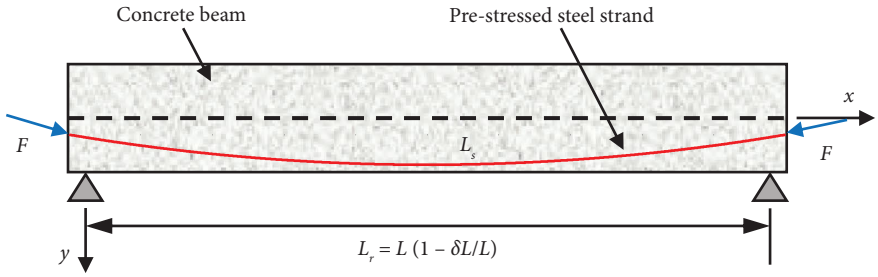

Figure 6: Mechanical model of the PSC girder.

$$f_n^2 = \left(\frac{n\pi}{L_r}\right)^4 \frac{E_r I_r}{m_r} = \left(\frac{n\pi}{L_r}\right)^4 \frac{1}{m_r}\left(E_c I_c + \left(\frac{L_s}{n\pi}\right)^2 F\right). \quad (12)$$

Equation (12) shows the prestressing force F can be calculated once f_n is determined:

$$F = \frac{f_n^2 L_r^4}{(n\pi L_s)^2} m_r - E_c I_c \left(\frac{n\pi}{L_s}\right)^2. \quad (13)$$

Equation (13) indicates that, theoretically, once the girder suffers prestress loss, a decrease in natural frequency can occur.

The relationship between dynamic response and the prestress state of PSC structures has also been experimentally investigated by several scholars, as shown in Table 4.

Table 4 indicates that there remain some controversies in the current studies on the relationship between natural frequency and prestress state of PSC structures. Some scholars suggested that the natural frequency of PSC structures is not influenced by prestress state or that there is no monotonous relationship between natural frequency and prestress state [119]. As early as 1991, Hop [113] investigated the effect of prestress degree on vibration of concrete beams, and results show vibration frequency firstly increases and then decreases with the increase in prestress. In addition, Hop stated that the most dominant factor affecting the natural frequency is the concrete cracking process, the stiffness of the beam decreases once concrete crack occurs, which in turn leads to a decrease in natural frequency. However, Hop did not explain the phenomenon that the natural frequency of the beam first increased and then decreased. Noble et al. [116] carried out dynamic impact experiments on 9 PSC beams with different eccentricities of prestressed strand; then, the first-order linear regression and statistical significance tests were subsequently conducted on the recorded data. Experimental results indicate that there is no statistically significant relationship between natural frequency and tension force for the 9 uncracked concrete beams. Similarly, Bonopera et al. [118] conducted 3 repeated laboratory experiments and demonstrated that the natural frequency was unaffected by changes in prestress, with only a 0.8% change in natural frequency when the increment of prestress was 17.7%. More experiments have proved a positive correlation between natural frequency and prestress state, but there remains some variation between these similar results. Saiidi et al. [111] carried out impact tests on a laboratory PSC girder and an in-service bridge. For the laboratory girder, both the first and second-order frequencies produced a significant increase with axial force; for the in-service bridge, the first-order frequency decreases with prestress loss, but the variation in frequency is quite slight, while the second-order frequency does not show a significant variation rule with prestress loss. In addition, Saiidi suggested that the application of prestress force makes the microcracks in the beam turn to close, which in turn leads to an increase in stiffness and the natural frequency. Gan et al. [120] utilized the finite element model to simulate the vibration response of a PSC beam in the presence of shrinkage cracks, and the results also demonstrate that the shrinkage cracks do tend to close when prestress is applied, thereby increasing the bending stiffness and natural frequency. Kim et al. [43] predicted the prestress loss of a PSC girder based on the measured natural frequency, and the predicted values were compared with actual ones, as shown in Figure 7. For the 1st–4th order modes, the prediction errors of prestress loss are 0–30%, 24–44%, 0–9%, and 0–33% respectively, which indicate that although the predicted prestress losses based on natural frequency are consistent with the actual ones, the predicted errors remain quite large.

Table 4: Research studies on prestress evaluation of PSC structures based on dynamic response.

Publication year	Researchers	Structural type	Research method	Acquisition method for vibration response	Experimental result
1991	Hop [113]	PSC beam	Laboratory experiments	Vibrograph, oscillograph	With the increase of prestressing force, the vibration frequency first increased and then decreased
1994	Saiidi et al. [111]	PSC beam	Field and laboratory experiments	Accelerometer	The first frequency slightly increased with the increase of prestressing force
2010	Kim et al. [43]	PSC T-shape girder	Laboratory experiment	Accelerometer	The natural frequency increased with the increase of prestressing force
2010	Kim et al. [114]	PSC beam	Laboratory experiment	Accelerometer	The longitudinal frequency showed a nonlinear increase with the increasing prestress
2011	Zhong et al. [115]	Box girder with vertical prestressed bars	Laboratory and field experiments	Accelerometer	The frequency increased with tension force
2012	Ho et al. [112]	PSC T-shape girder	Laboratory experiment	Accelerometer	The natural frequency increased with the increase of prestressing force
2016	Noble et al. [116]	PSC beam	Laboratory experiment	Accelerometer	No statistically significant relationship between natural frequency and posttensioning load level were found
2018	Rashetnia et al. [117]	PSC beam	Laboratory experiment	Accelerometer	The use of dynamic vibration can quantify the loss of prestressing force
2019	Bonopera et al. [118]	PSC beam	Laboratory experiment	Velocity seismometer	No change in fundamental frequency with increasing prestressing force

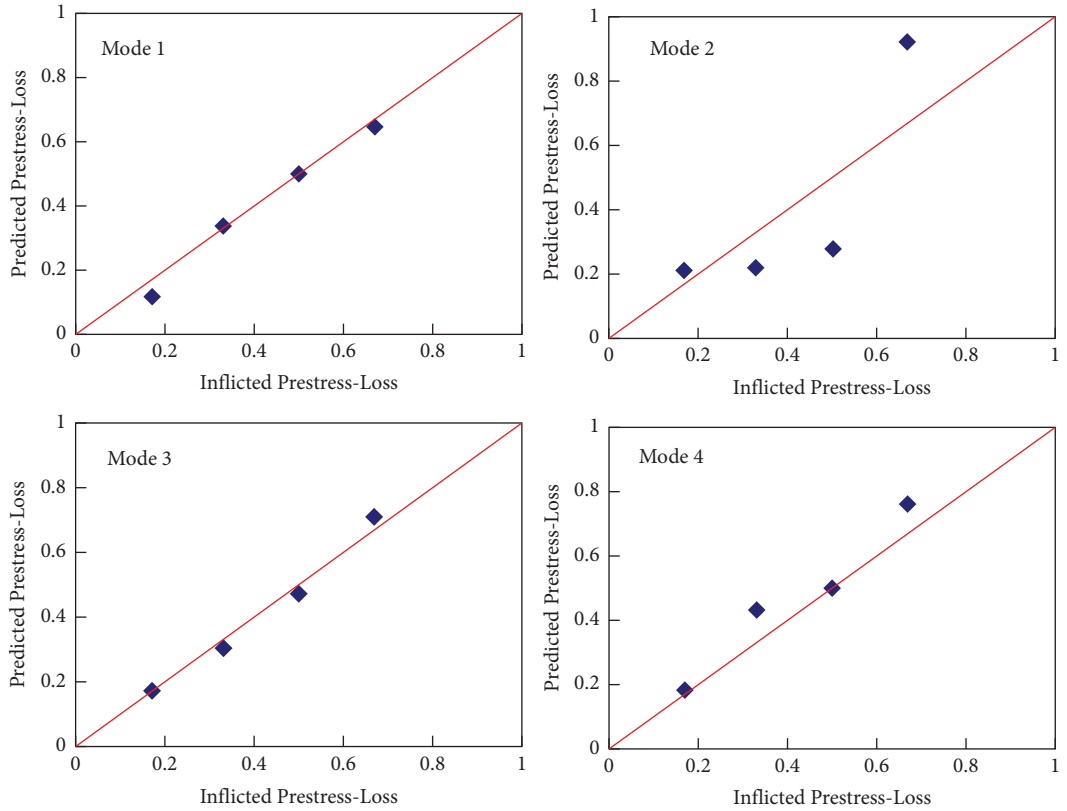

Figure 7: Prediction of prestress losses in PSC girder (in the research of Kim et al. [43]).

In summary, in terms of dynamic response-based prestressing force estimation for PSC structures, there is no consensus on the relationship between the variation of prestress and natural frequency, either in theoretical calculations or in experimental experiments. Most of the relevant studies are still at the laboratory investigation stage and have not yet been applied to practical engineering.

In conclusion, the dynamic response-based method has been widely implemented in cable force estimation, and the measuring error can be limited to less than 10%. However, there remain several difficulties in prestress estimation for PSC structures. This can be attributed to the differences in force state and boundary condition between the cable and PSC structure. The cable is mainly subjected to axial forces, and its boundary conditions are relatively simple; that is, only the hinged or tied constraints at the ends of the cable need to be considered. Therefore, the equations for calculating cable force are easy to solve. In addition, the cable is directly exposed to the external environment and its vibration is relatively independent, which makes the dynamic response easy to monitor. In the case of PSC structure, the force state is complex; the steel strand bears the tension force, and the concrete bears the compression force. Meanwhile, how to consider the prestress effect in the differential equation of motion for PSC structures has not yet reached a unified understanding.

2.4. UGW-Based Method. The main difference between UGW and ultrasonic testing is that UGW propagates directionally along with the medium and takes advantages of low signal attenuation and long propagation distances. UGW is considered a viable approach for structural stress detection, which has been applied to stress detection in railway rails [121], concrete [122], as well as bolt preload [123, 124]. Some scholars have also employed UGW for structural prestress estimation. According to the research studies, the main approaches based on the UGW technique include the acoustoelastic effect-based approach [125], missing frequency band-based approach [126], and singular value feature-based approach [127].

In the UGW-based method, two vital characteristics must be concerned, namely, dispersion and multimodes [128]. The dispersion refers to the variation of wave velocity with frequency. The multimode property means that there are three modes in propagation: longitudinal, flexural, and torsional, each of which contains multiple orders. Both characteristics can be reflected in the dispersion curves. In terms of steel strands, the dispersion curves for the core wire are shown in Figure 8.

2.4.1. Acoustoelastic Effect-Based Approach. The wave velocity of UGW can be changed with structural stress state, which is called acoustoelastic effect [129, 130]. For a uniform isotropic infinite solid subjected to uniaxial stress, the

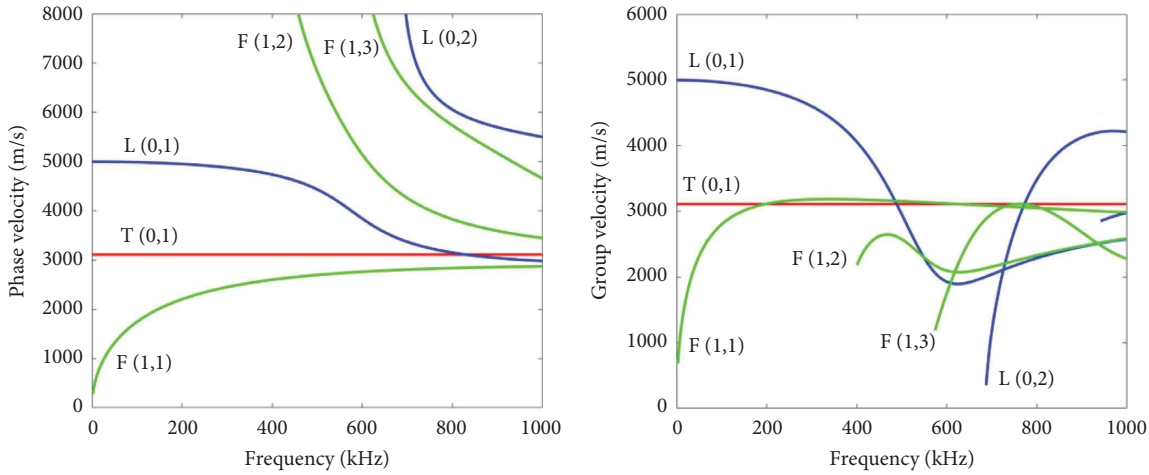

Figure 8: Dispersion curves for the core wire of prestressed steel strand: (a) phase velocity and (b) group velocity.

velocities of longitudinal and transverse waves propagating in the same direction as the stress can be expressed as follows:

$$V_L^\sigma = V_L^0(1 + K_L\sigma),$$
$$V_T^\sigma = V_T^0(1 + K_T\sigma), \tag{14}$$

where V_L^σ and V_T^σ refer to velocities of longitudinal and transverse waves at stress σ, V_L^0 and V_T^0 refer to velocities of longitudinal and transverse waves at stress-free state, and K_L and K_T refer to longitudinal and transverse acoustoelastic coefficients and can be calculated as

$$K_L = \frac{1}{2(\lambda + 2\mu)(3\lambda + 2\mu)}\left(\frac{\lambda + \mu}{\mu}(4\lambda + 10\mu + 4m) + \lambda + 2l\right),$$
$$K_T = \frac{1}{2\mu(3\lambda + 2\mu)}\left(4\lambda + 4\mu + m + \frac{\lambda n}{4\mu}\right), \tag{15}$$

where λ and μ refer to Lame's elastic constants and m, l, and n refer to Murnaghan's third-order elastic constants. In addition to theoretical calculation, the acoustoelastic coefficients can be determined from laboratory calibration tests. Previous studies show that the effect of stress level on wave velocity is relatively small; therefore, a device with higher accuracy is required to measure the change in wave velocity in experimental calibration tests [131].

Several scholars have carried out research studies on acoustoelastic effect-based structural prestress evaluation. Chaki and Bourse [132] calibrated the acoustoelastic coefficient of a 7-wire steel strand based on the L (0, 1) mode of UGW, and the result is shown in Figure 9. Notably, the phase velocity of L (0, 1) mode exhibits a nonlinear relationship with prestress when the stress is below 600 MPa. Subsequently, the prestress state was calculated according to the acoustoelastic coefficient obtained from calibration:

$$\sigma = \frac{1}{K}\left(\frac{l_t - t_t V_0}{t_t V_0 - l_u}\right), \tag{16}$$

where K refers to the calibration value of the acoustoelastic coefficient, l_t refers to the total length of the strand, i.e., the sum of the stressed part and stress-free part, l_u refers to the length of stress-free part outside the anchored end of the strand, V_0 refers to phase velocity at stress-free state, and t_t refers to time-of-flight of UGW propagating in the strand. Chaki claimed that the errors between estimated prestress values and the actual ones are small; for example, the applied stress value is 1339 MPa at 72% of the ultimate tensile strength, while the estimated one is 1330 MPa. However, equation (16) indicates that the measuring error in strand length can strongly influence the estimated result. In this study, the range of measuring error in strand length is ±1 mm, which can lead to an estimated prestress error of ±123 MPa. Therefore, in the acoustoelastic effect-based approach, prestress estimation deviations caused by measuring errors in strand length are likely to result in distortion of prestress estimation.

Similarly, Dubuc et al. [125] investigated the effect of axial stress on the propagation behavior of longitudinal higher-order modes of UGW for prestressed steel strands, and the measuring results were compared with theoretical calculation ones, as shown in Figure 10. There is a certain degree of deviation (about 15%) between measuring results and theoretical ones, which is mainly due to uncertainty in the value of Murnaghan's third-order elastic constants.

2.4.2. Missing Frequency Band-Based Approach. The missing frequency band refers to the energy in a certain frequency band of UGW producing a serious attenuation when UGW propagates in steel strand under axial tension, which shows a missing band in the frequency domain.

The missing frequency band of UGW was first discovered by Kwun et al. [133]. They investigated the effect of tensile loading on the properties of longitudinal-mode UGW

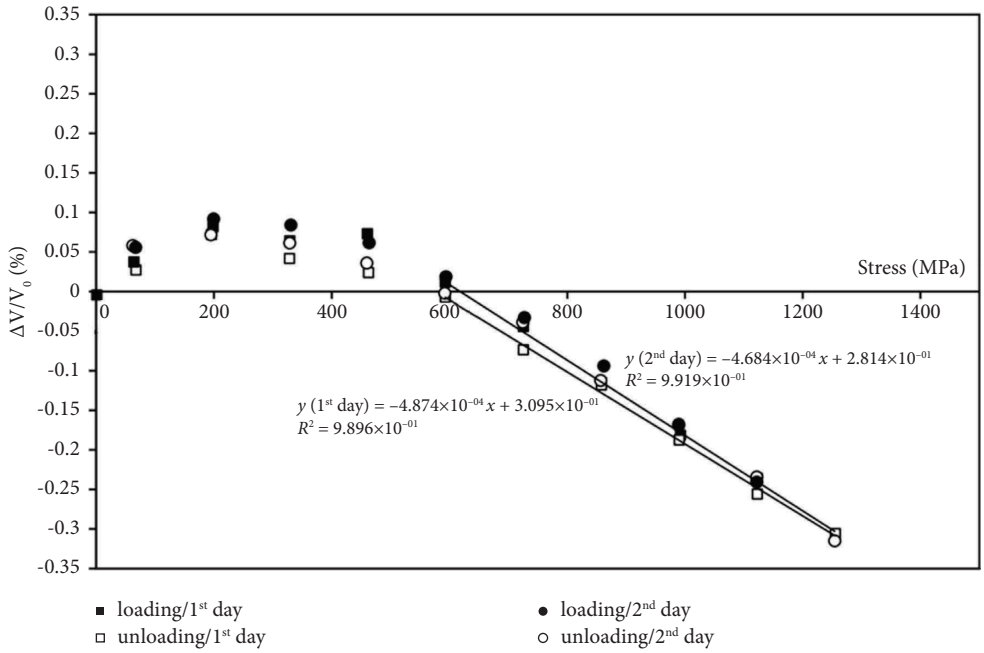

Figure 9: Acoustoelastic calibration curves in Chaki's and Bourse research [132].

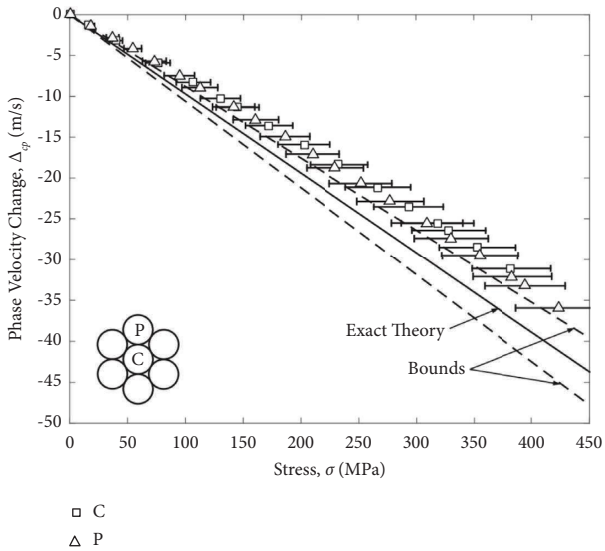

Figure 10: Experimental phase velocity change for the L (0, 9) mode in the core and peripheral wire in Dubuc et al.'s research [125].

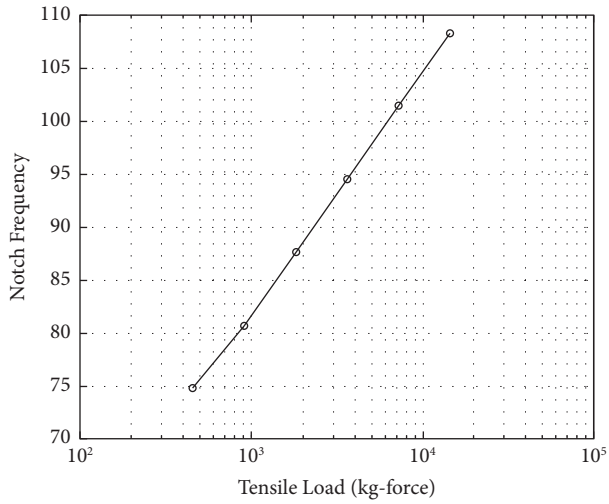

Figure 11: A plot of missing frequency versus applied tensile load to a seven-wire prestressed strand with a 12.7 mm nominal diameter [133].

in prestress steel strands. The time-frequency spectrum shows a serious attenuation at 75 kHz when tensile force reaches 10% of the nominal yield strength, i.e., a missing band is generated. The center frequency of missing band gradually shifts to the right with the increase in tensile force, as shown in Figure 11. There is a strong linear relationship between center frequency of missing band and logarithm of tensile force (i.e., logN), which provides a new idea for the UGW-based prestress evaluation method.

Treyssède [134] utilized semianalytical finite element (SAFE) to analyze the missing frequency band, and the relationship between frequency missing band and tensile force is highly consistent with experimental results by Kwun et al. [133]. Treyssède et al. [134] explained that the missing frequency band was caused by the increase in contact width between core wire and helical wire. The change in interwire contact breaks the circular symmetry of the wire cross-section, thus yielding coupling between longitudinal, flexural, and torsional motion together with curve veering phenomena.

According to the missing frequency band of UGW, Liu et al. [135] proposed a new parameter to evaluate effective prestress for steel strands. This new parameter refers to the amplitude ratio of two peaks on the left and right sides of the missing frequency band, and the relationship between

amplitude ratio and tensile force is shown in Figure 12. The amplitude ratio increases linearly with tensile force with a fitting accuracy $R^2 = 0.9952$ and within a maximum error of 10%.

2.4.3. Singular Value Feature-Based Approach. As an attractive signal processing method, singular value decomposition has been applied in UGW-based defect localization and damage detection [136, 137]. Ji et al. [127] first applied singular value decomposition in the UGW-based prestress evaluation method with the following process: (1) wavelet packet transform (WPT) is performed on the time domain signal of UGW to obtain the wavelet packet coefficient matrix; (2) singular value decomposition of the wavelet packet coefficient matrix is performed to obtain the singular value vector which reflects the stress characteristics in the time and frequency domain; (3) a support vector regression model is constructed using the singular value vector as input and the prestress level as output. The predicted prestress based on the above process is shown in Figure 13. The error between predicted prestress values and actual ones is basically within ±5%, and the prediction accuracy increases with the size of training sets.

In summary, an unavoidable problem in the acoustoelastic effect-based approach is that the measuring error in strand length can strongly influence the estimated result, thus resulting in distortion of prestress estimation. In addition, the acoustoelastic effect-based approach only analyzes the difference of the UGW signal in the time domain, while numerous research studies have shown that the frequency domain spectrum and the time-frequency spectrum contain a large amount of information related to the structural state. Both the missing frequency band and singular value evaluate the prestress state based on frequency domain or time-frequency domain features with high measuring accuracy. Therefore, compared with the acoustoelastic effect-based approach, the missing frequency band-based approach and singular value feature-based approach are more suitable for prestress evaluation, although some engineering cases are needed to verify their feasibility and accuracy in the field.

2.5. EMI-Based Method. The principle of structural damage assessment based on EMI can be summarized as follows [138]: In the application of the EMI technique, a sensor made of piezoelectric material, e.g., PZT, is required to be attached to the surface of the measured structure. A sinusoidal alternating voltage excitation is applied to the piezoelectric element; due to the inverse piezoelectric effect, the piezoelectric element generates a forced vibration and transmits the vibration to the structure. Simultaneously, the vibration of the structure in turn deforms the piezoelectric element and changes the current in the circuit due to the positive piezoelectric effect. In terms of the electromechanical system coupled by the piezoelectric element and the structure, the changes in structural natural

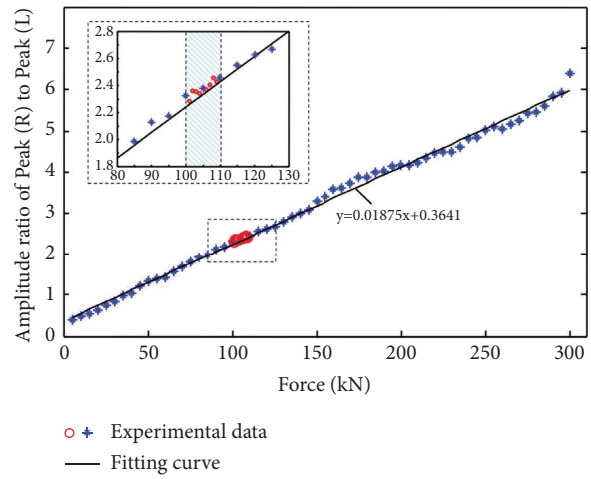

Figure 12: Relationship between the amplitude ratio of peak (R) to peak (L) and the tensile force of a seven-wire steel strand [135].

properties, such as stiffness, can lead to a change in its EMI. Therefore, structural damage identification can be achieved by monitoring impedance changes in the electromechanical system.

Benefiting from the advantages of high operating frequency and sensitivity to local damage, the EMI technique has been broadly employed in damage monitoring for rocks [139], concrete [140, 141], metals [142], composite structures [143], and material corrosion [144, 145]. In addition, some scholars have also applied the EMI technique to the evaluation of the structural prestress, as shown in Table 5.

Figure 14 shows the diagram for the EMI-based method [146]. As shown in Figure 14(a), a PZT patch is attached to the bearing plate at the anchor end. The PZT patch can be equivalent to a combination of three parameters, namely, mass (m^i), stiffness (k^i), and damping (c^i); similarly, the bearing plate is equivalent to a combination of mass (m^b), stiffness (k^b), and damping (c^b); the contact of bearing plate and PSC structure is equivalent to a spring with stiffness k and damping c. The change in prestress can result in changes in the spring, mass, and stiffness of the contact interface. The dynamic coupling response of the PZT and PSC structure can be simplified to a 2-DOF impedance model, as shown in Figure 14(b); Z_s, Z_i, and Z_a refer to impedances of the anchoring system, PZT interface, and PZT patch, respectively, and $\overline{Z}$ refers to the sum of Z_s and Z_i. The impedance of the whole system consisting of PZT, PZT interface, and anchorage can be calculated as

$$Z(\omega) = \frac{V}{I} = \left\{ i\omega \frac{w_a l_a}{t_a} \left[\widehat{\varepsilon}_{33}^{T} - \frac{1}{Z_a(\omega)/\overline{Z}(\omega) + 1} d_{31}^2 \widehat{Y}_{11}^{E} \right] \right\}^{-1}, \tag{17}$$

where V refers to the input excitation voltage, I refers to the output current, $Z(\omega)$ refers to impedance of the whole system, $\widehat{Y}_{11}^{E}$ refers to the complex Young's modulus of the PZT patch at zero electric field, $\widehat{\varepsilon}_{33}^{T}$ refers to the complex dielectric constant at zero stress, d_{31}^2 refers to the piezoelectric coupling constant at zero stress, ω refers to the

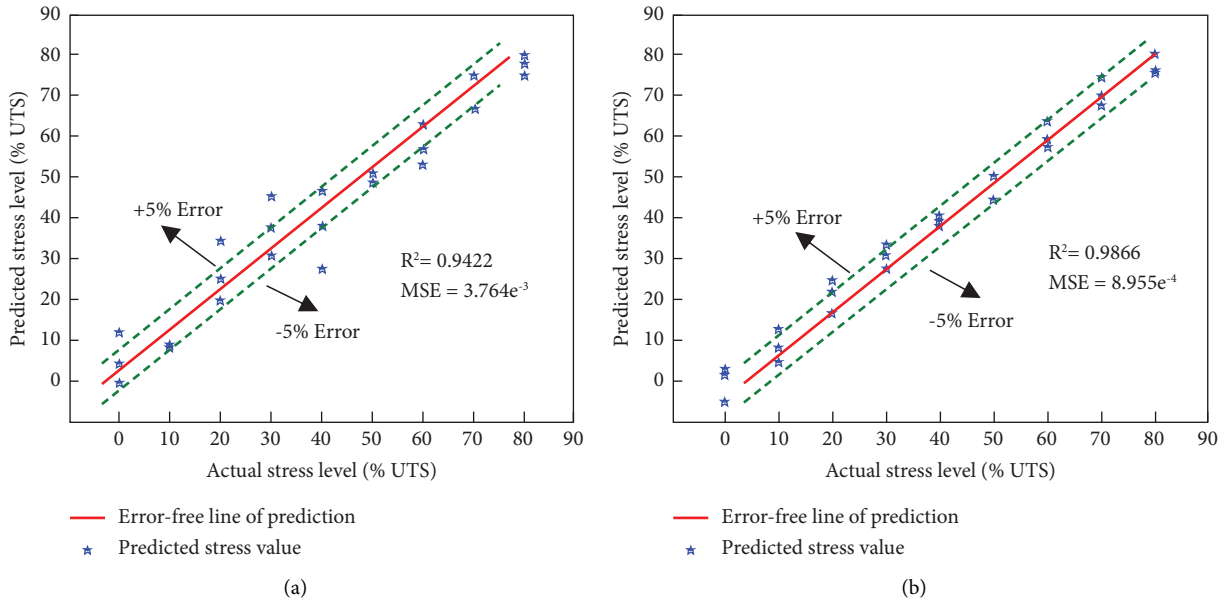

Figure 13: Prediction of stress status with (a) small samples and (b) additional samples [127].

excitation frequency, and w_a, l_a, and t_a refer to the width, length, and thickness of the PTZ patch, respectively. The impedance of the whole system can vary with prestress or environmental temperature. Therefore, it is feasible in principle to utilize the variation in impedance to calculate the change in prestress.

In the research studies of Huynh and Kim, two damage indexes, namely, root mean square deviation (RMSD) and correlation coefficient deviation (CCD), were introduced to quantify the local damage of PSC structure caused by prestress loss [149]:

$$\mathrm{CCD} = 1 - \frac{1}{\sigma_Z \sigma_Z^*} E\left\{\left[\mathrm{Re}\left(Z\left(\omega_i\right)\right) - \mathrm{Re}\left(\overline{Z}\right)\right]\left[\mathrm{Re}\left(Z^*\left(\omega_i\right)\right) - \mathrm{Re}\left(\overline{Z}^*\right)\right]\right\}, \tag{18}$$

where $E[.]$ refers to the expectation operation, $Z(\omega_i)$ and $Z^*(\omega_i)$ refer to impedances at the ith frequency before and after damage, $\overline{Z}$ and $\overline{Z}^*$ refer to the mean value of $Z(\omega_i)$ and $Z^*(\omega_i)$, and σ_Z and σ_Z^* refer to the standard deviation of $Z(\omega_i)$ and $Z^*(\omega_i)$.

$$\mathrm{RMSD} = \sqrt{\sum_{i=1}^{N}\left[Z^*\left(\omega_i\right) - Z\left(\omega_i\right)\right]^2 / \sum_{i=1}^{N}\left[Z\left(\omega_i\right)\right]^2}, \tag{19}$$

where N refers to the number of swept frequencies. In addition, a damage warning threshold, i.e., the upper control limit (UCL), is proposed for the statistical damage classification:

$$\mathrm{UCL} = \mu + 3\sigma, \tag{20}$$

where μ and σ refer to the mean and standard deviation of UCL. According to the 3σ criterion, the damage probability is greater than 99.73% if damage index is higher than UCL. The prestress loss inspection results based on damage indexes and UCL are shown in Figure 15, CCD and RMSD increase significantly as the PSC girder suffers prestress loss, and UCL effectively provides early warning of the occurrence of prestress loss.

As mentioned above, changes in both structural prestress state and environmental temperature cause change in the impedance of the anchored end. Therefore, incorrect judgment of prestress loss may occur if the contribution of temperature variation to structural impedance is ignored. To explain the mechanism of the effect of temperature variation on the impedance, Huynh and Kim [147] constructed a finite element model of the PSC girder with anchorage end and investigated the stress field at the anchorage end under the effect of prestress and thermal effects. The changes in local stress at the PZT interface caused by prestress and temperature are shown in Figure 16, and the PZT interface is compressed in the longitudinal direction with the increase of prestress and temperature, thus stiffening the PZT interface and increasing in resonant frequencies (i.e., the stiffening effect). In this regard, they proposed a temperature compensation approach based on effective frequency shift (EFS). The EFS approach obtains the baseline impedance spectrum by shifting the frequency change $\delta\omega_{\delta T}$ generated by the temperature change δT, and

Table 5: Research studies on structural prestress evaluation based on the EMI technique.

Publication year	Researchers	Structural type	Laboratory or field	Sensor type	Sensor position	Research focus	Measuring error
2012	Nguyen and Kim [42]	PSC girder	Laboratory	PZT	Anchorage plate	Presenting a wireless EMI-based prestress monitoring system	With a maximum error of 9.8%
2017	Huynh and Kim [146]	PSC girder	Laboratory	PZT	Anchorage plate	Proposing a phase-by-phase model updating algorithm to quantitatively identify the prestress loss	—
2017	Huynh and Kim [147]	PSC girder	Laboratory	PZT	Anchorage plate	Proposing an effective frequency shift-based algorithm to filter temperature effects	—
2018	Huynh et al. [148]	PSC girder	Laboratory	PZT	Anchorage plate	Proposing a PCA-based algorithm to filter temperature effects	—
2018	Huynh and Kim [149]	PSC girder	Laboratory	PZT	Anchorage plate	Proposing an RBFN-based algorithm to monitor prestress change under temperature variation	—
2019	Ryu et al. [150]	Steel strand	Laboratory	PZT	Surface of the strand	Proposing a novel wearable PZT interface to monitor prestress change	—
2020	Dang et al. [151]	Multiple steel strands	Laboratory	PZT	Anchorage plate	Determining optimal locations of PZT sensors for prestress monitoring	—
2021	Dang et al. [152]	Multiple steel strands	Laboratory	PZT	Anchorage plate	Designing a hoop-type PZT interface	—
2021	Le et al. [153]	PSC girder	Laboratory	PZT	Surface of the strand	Presenting a smart strand prepared by embedding inexpensive and high-sensitivity EMI sensor	—

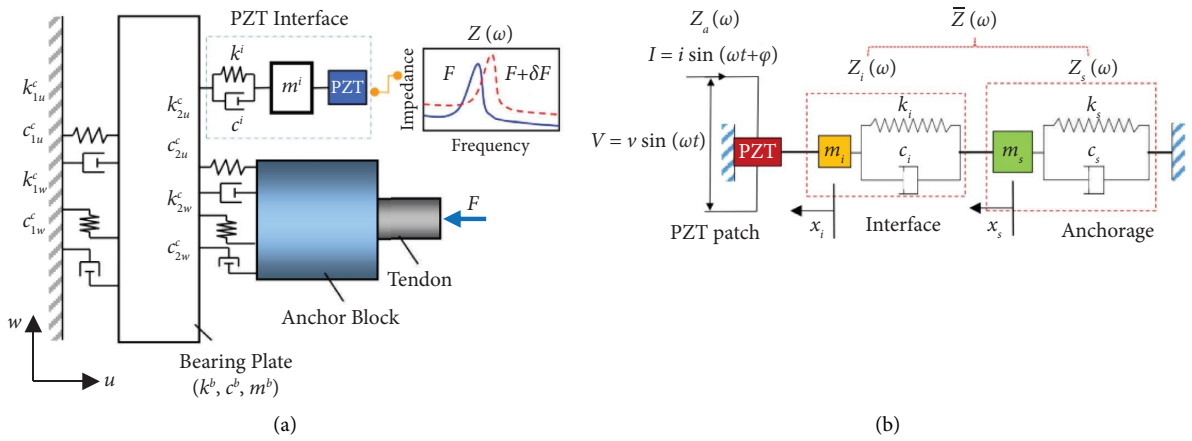

FIGURE 14: Analytical impedance model of the PZT interface-tendon anchorage system [146]. (a) Equivalent structural model of PZT interface-tendon anchorage. (b) 2-DOF impedance model.

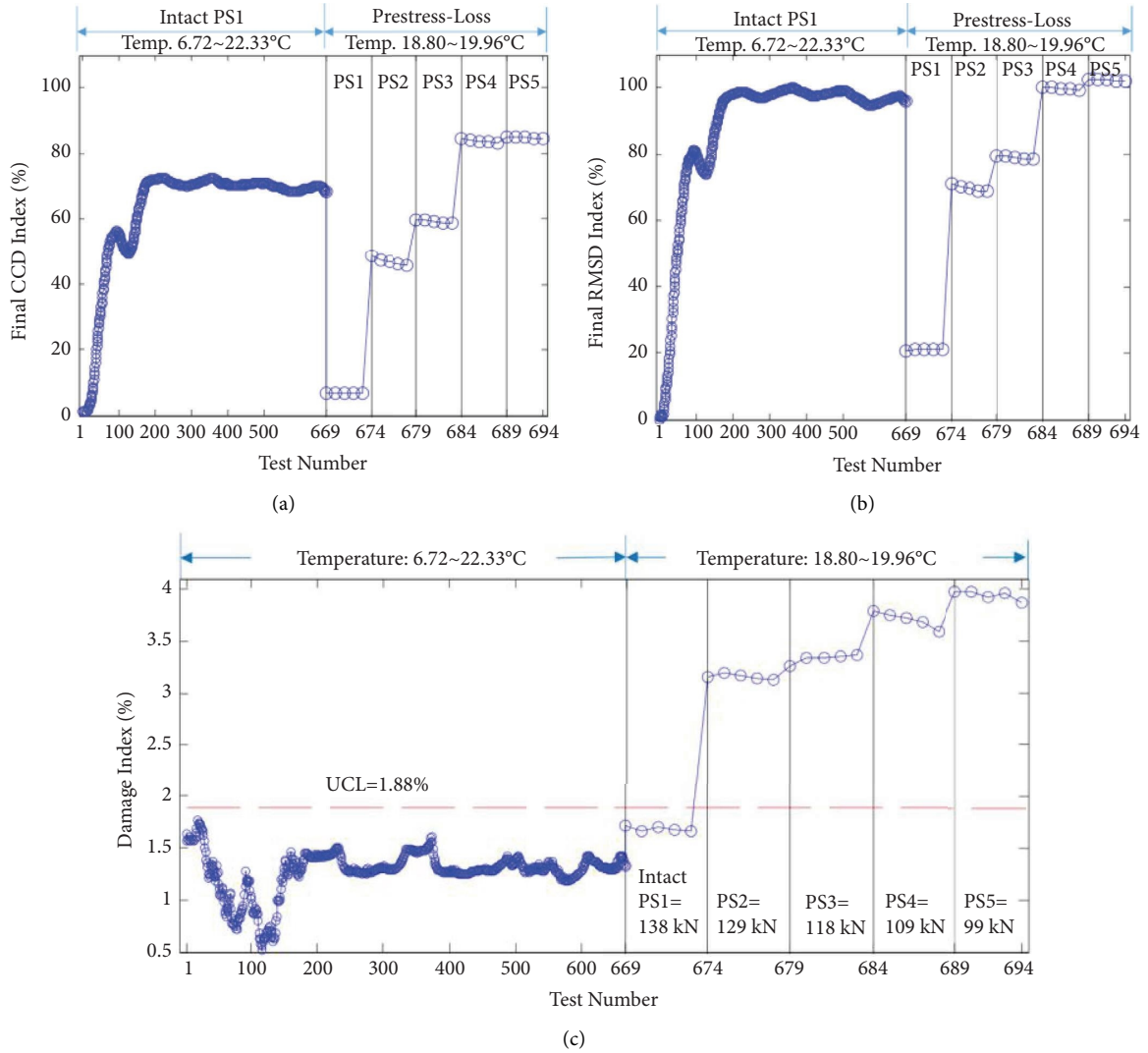

FIGURE 15: Prestress-loss inspection using (a) CCD index, (b) RMSD index, and (c) UCL [147].

the prestress loss is accurately predicted based on temperature-compensated impedance by the EFS approach. In addition, a principal component analysis (PCA)-based approach [148] and a radial basis function network (RBFN)-based approach [149] were also proposed for temperature compensation of the EMI technique. In the PCA-based approach, the damage indexes (i.e., RMSD and CCD) caused by temperature variations are calculated first; then, the damage index matrix is constructed and principal components in the matrix are extracted; finally, the impedance variations due to the temperature effect are successfully filtered out by removing the two principal components (i.e., PC1 and PC2) that contribute most to the temperature variation. In the RBFN-based approach, impedance spectrums under varying temperatures and corresponding temperature values are input to the network and temperature-compensated impedance baseline spectrums are output. Results show that the error between the baseline impedance spectrums using the RBFN approach and measured impedance spectrums under the reference temperature is negligible if the number of training samples is enough (more than 168).

Apart from investigating the effect of temperature on prestress estimation results, the optimal placement of PZT patches at the anchor end is also studied, which is related to the sensitivity of stress field at the anchor end to changes in prestress. Dang et al. [151] investigated the local prestress variation at the anchor end by attaching axial, circumferential, and radial strain gauges. Results show that the near top of the anchor head is more sensitive to circumferential stress change, while the near bottom of the anchor head is more sensitive to axial stress change. Subsequently, three PZT patches were attached at the top, middle, and bottom of anchor head and one was attached at the bearing plate to monitor local damage due to prestress variations, as shown in Figure 17(a). Results indicate that the near top and near bottom of anchor head are ideal areas for measuring prestress loss. To monitor and locate local fracture and prestress loss in the multi-strand anchorage system, Dang et al. [152] proposed a hoop-type PZT patch and a circumferential PZT arrangement, as shown in Figure 17(b). The PZT patches were attached to the top and bottom of the anchor head, and the circumferential positions corresponded to the positions of peripheral strands. The experimental results show that PZT patches are only sensitive to prestress damage of the nearest peripheral strand, while the prestress damage of center strand cannot be effectively monitored. In addition to attaching PZT patches on the anchor end surface, Ryu et al. [150, 153] also designed a PZT fixed to strand surface, as shown in Figure 18, the patch was fixed to the strand through connecting rings at both ends, and PZT arranged in this way is also effective in prestress monitoring for steel strand.

In summary, the EMI-based method is effective in prestress monitoring in laboratory experiments. However, since no reports or literature works on the field application have been found, its field applicability needs to be further verified. In addition, as EMI is locally sensitive, the PZT patch may only monitor prestress loss occurring at the anchorage end while not enabling monitoring prestress losses due to concrete shrinkage, creep, and duct friction.

2.6. Electrical Resistance-Based Method. Electrical resistance is an essential property of a material that may be changed if damage occurs. Accordingly, structural damage assessment can be performed through electrical resistance monitoring. Indeed, it has been employed in the evaluation of metal corrosion [154], durability [155], and cracks [156] of concrete.

The volume contraction and plastic deformation of the metal caused by external stress will change the resistivity, and changes in resistivity and volume will further lead to a change in electrical resistance. It has been demonstrated that resistivity variation shows great potential in predicting the tensile strength of metal [157]. Therefore, it should also be feasible to evaluate the structural prestress state using the change in resistance or resistivity. Zhang et al. [35] conducted a preliminary study on electrical resistance-based prestress evaluation method, and the principle is described as follows.

Taking the 7-wire strand as an example, the stress σ_c under axial tensile force F can be expressed as

$$\sigma_c = \frac{F}{A_c + 6A_h \cos^3 \beta}, \tag{21}$$

where A_c and A_h refer to the cross-sectional areas of core wire and helical wire, respectively, and β refers to the lay angle of helical wire. According to the classical Ramberg–Osgood model, the strain of core wire can be expressed as

$$\varepsilon_c = \varepsilon_{ce} + \varepsilon_{cp} = \frac{\sigma_c}{E} + 0.002\left(\frac{\sigma_c}{\sigma_{0.2}}\right)^n, \tag{22}$$

where ε_c, ε_{ce}, and ε_{cp} refer to total strain, elastic strain, and plastic strain, E refers to the elastic modulus, $\sigma_{0.2}$ refers to the stress corresponding to 0.2% plastic strain, and n refers to the hardening index. The change in tensile fore of core wire leads to changes in its length and cross-section, which can be expressed as

$$\begin{aligned} \frac{\mathrm{d}r_c}{r_c} &= -\nu \frac{\mathrm{d}l_c}{l_c} \\ &= -\nu\varepsilon_c \Longrightarrow r_{cT} \\ &= r_c\left(1 - \nu\varepsilon_c\right) \Longrightarrow A_{cT} \\ &= \pi r_c^2 \left(1 - \nu\varepsilon_c\right)^2, \end{aligned} \tag{23}$$

where r_c and l_c refer to initial radius and length, dr_c and dl_c refer to changes in radius and length, ν refers to the Poisson ratio, and A_{cT} refers to cross-sectional area of tensed core wire. Changes in length and cross-sectional area lead to a change in resistivity, ρ:

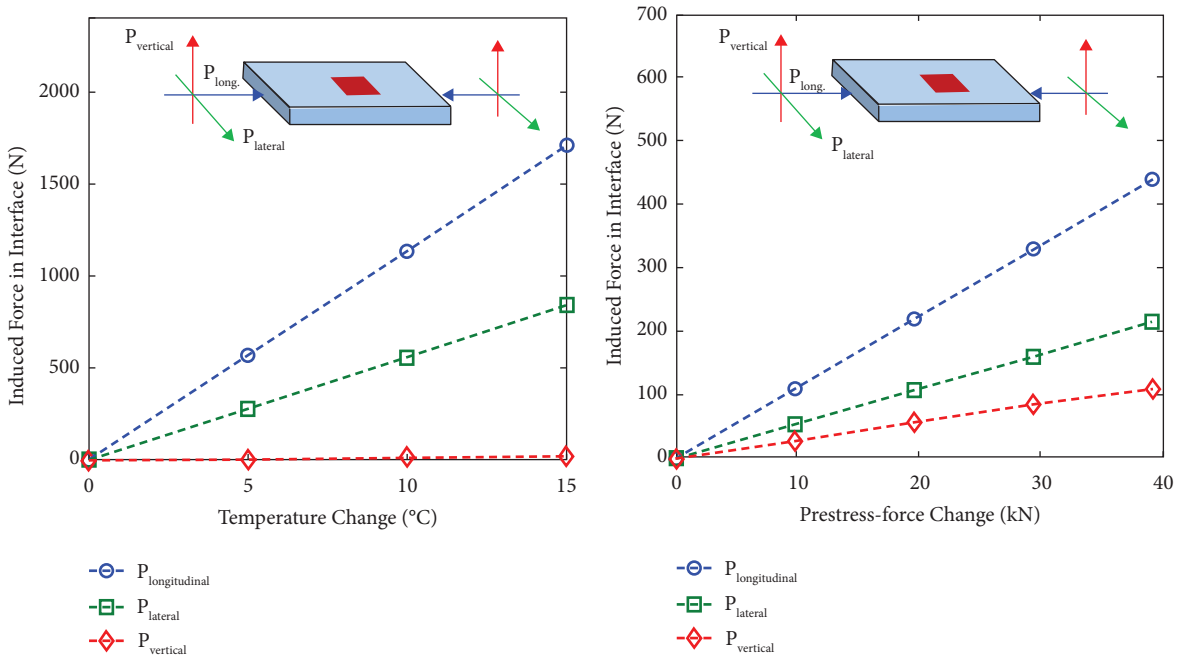

Figure 16: Induced forces in PZT interface due to temperature variation and prestress change [147]. (a) Temperature variation. (b) Prestress-force change.

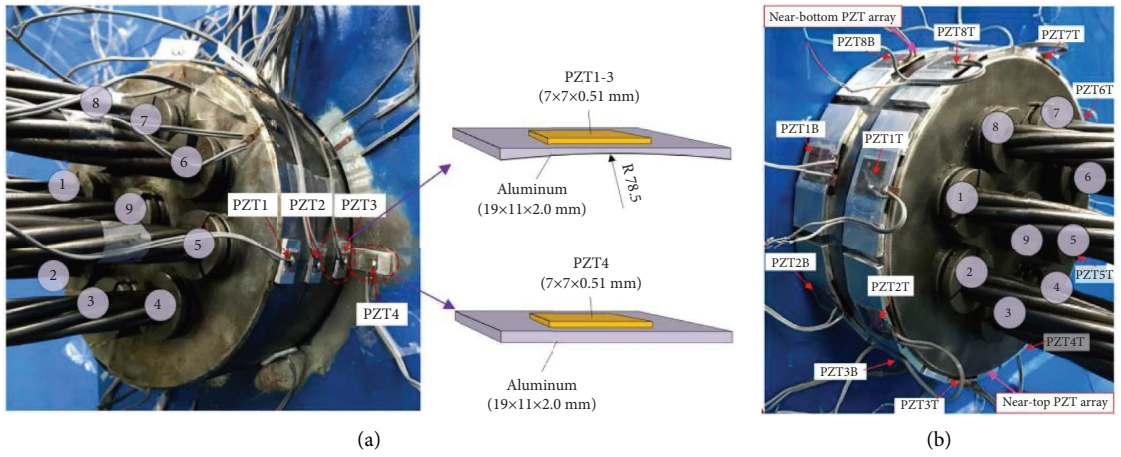

Figure 17: Layout of PZT patches in the anchorage system. (a) PZT patches on the anchorage [151]. (b) Hoop-type PZT patches [152].

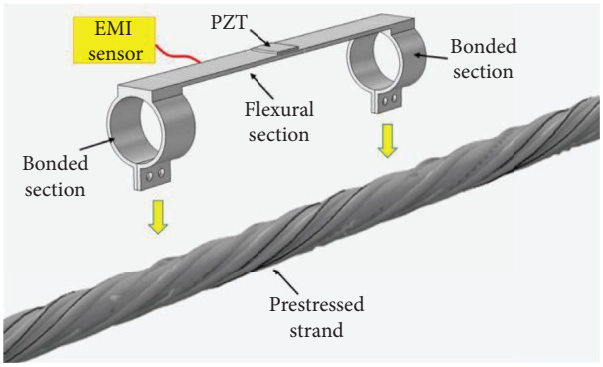

Figure 18: Diagram of PZT patches attached to the prestressed steel strand [153].

$$\begin{aligned}\frac{\Delta\rho_{cV}}{\rho_c} &= C_1\frac{\Delta V_c}{V_c}\\ &= C_1\frac{l_c(1+\varepsilon_c)\cdot\pi r^2(1-\nu\varepsilon_c)^2 - V_c}{V_c}\\ &= C_1\left[(1+\varepsilon_c)(1-\nu\varepsilon_c)^2 - 1\right],\end{aligned} \tag{24}$$

where ρ_c refers to initial resistivity, $\Delta\rho_{cV}$ refers to resistivity increment caused by volume change, and C_1 refers to a constant. The resistivity change caused by plastic deformation can be calculated as

$$\frac{\Delta\rho_{cp}}{\rho_c} = C_2\varepsilon_{cp}^{n_2}, \tag{25}$$

where $\Delta\rho_{cp}$ refers to resistivity increment caused by plastic deformation and C_2 and n_2 refer to constants. The electrical resistance change is determined by both changes in volume and resistivity:

$$\begin{aligned}R_{cT} &= \rho_{cT}\frac{l_{cT}}{A_{cT}}\\ &= \rho_c\left(1+\Delta\rho_{cV}+\Delta\rho_{cp}\right)\frac{l_c(1+\varepsilon_c)}{A_c(1-\nu\varepsilon_c)^2}\\ &= \left\{1+C_1\left[(1+\varepsilon_c)(1-\nu\varepsilon_c)^2-1\right]+C_2\varepsilon_{cp}^{n_2}\right\}\frac{(1+\varepsilon_c)}{(1-\nu\varepsilon_c)^2}\cdot R_c,\end{aligned} \tag{26}$$

where R_{cT} and ρ_{cT} refer to electrical resistance and resistivity of tensed core wire and R_c refers to initial electrical resistance. The change of electrical resistance caused by volume may be more than that caused by resistivity. If the change in resistivity was ignored, equation (26) can be simplified as

$$\frac{R_{cT}}{R_c} = \frac{(1+\varepsilon_c)}{(1-\nu\varepsilon_c)^2}. \tag{27}$$

In the measuring process, since the resistivity of steel strand changes little, the resistivity of the full strand is equivalent to the resistivity of the part stretched out of anchors, which can be measured in advance. Therefore, the initial electrical resistance can be calculated as

$$\begin{aligned}\frac{R_{cd}}{R_c} &\approx \frac{\rho_{cT}(l_{cd}/A_{cd})}{R_{cd}} = \frac{(1+\varepsilon_{cd})}{(1-\nu\varepsilon_{cd})^2} \Longrightarrow R_c\\ &= \rho_{cT}\frac{l_{cd}(1-\nu\varepsilon_{cd})^2}{\pi r_c^2(1-\nu\varepsilon_{cd})^2(1+\varepsilon_{cd})}\\ &= \rho_{cT}\frac{l_{cd}}{\pi r_c^2(1+\varepsilon_{cd})},\end{aligned} \tag{28}$$

where R_{cd}, l_{cd}, A_{cd}, and ε_{cd} refer to electrical resistance, length, cross-sectional area, and strain under designed tensile force, which are known parameters. Therefore, the unknown stress state can be obtained if the corresponding electrical resistance R_{cT} is measured using equations (22) and (27).

Based on the above calculation theory, Zhang et al. [35] proposed an equivalent circuit model for 7-wire prestressed steel strands: in terms of epoxy-coated strand, the wires are equivalent to resistances insulated from each other; while in terms of galvanized-coated strand, the wires conductive to each other form a parallel resistance R_s, as shown in Figure 19. In the experiment, conducting wires were welded to the end of the helical wire to connect the ammeter and voltmeter, and the strand resistance was obtained by dividing the measured voltage by the measured current. Results show that the effective prestress can be calculated by the fitting function of incremental resistance ΔR and tensile force F, and the error between estimated and true values of the tensile force is about 10%.

In summary, the electrical resistance-based method shows excellent potential for structural prestress evaluation. However, since this is only a preliminary study, several factors, such as thermal effect, have not yet been considered. More in-depth studies for this method are needed if engineering applications are to be realized.

3. Challenges and Discussion for Future Research

Based on the review of various prestress evaluation methods mentioned above, the current understanding has been synthesized, and the main challenges and discussion for future research are identified in the following four aspects: measuring range, reliability of measuring results, stability and durability considering long-term monitoring, and cost-efficiency. Subsequently, a decision tree is proposed to choose the most appropriate prestress evaluation method in a specific application scenario.

3.1. Measuring Range. In terms of the FBG sensor-based method, it is well known that conventional FBG sensors can only obtain stress data from a limited number of measuring points [40], while the stress distribution along the full strand length cannot be measured. The Brillouin optical time domain reflection (BOTDR) sensing technique enables strain and temperature distribution over the full structural length by measuring the Brillouin frequency shift along the fiber length [158]. Related studies have proved the effectiveness of smart strands with embedded BOTDR sensors in monitoring prestress distribution [51]. However, the BOTDR sensing-based technique has not been applied in practical engineering yet, which may be due to the low spatial resolution of BOTDR sensors. Therefore, improvement in spatial resolution of BOTDR sensors can be considered in future research. In terms of the dynamic response-based method, one accelerometer can only measure the cable force of a single cable [85, 99], while microwave interferometric radar-based [94] and image-based [102] approaches can achieve simultaneous measurement of multiple cable forces, which is obviously more in line with practical engineering needs and more promising for promotion. As for the

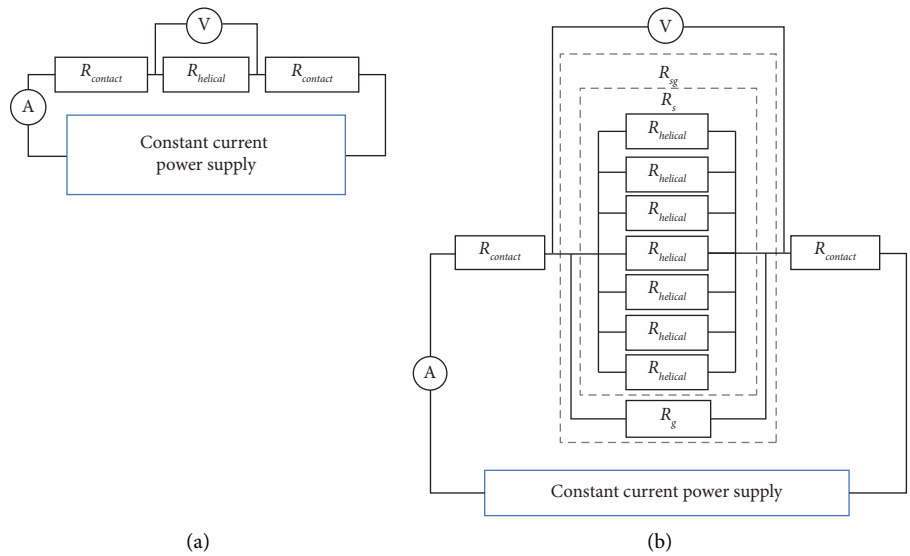

Figure 19: Equivalent electrical model of prestress testing [35]. (a) Epoxy-coated steel strand. (b) Galvanized steel strand.

UGW-based method, although one of the advantages of the UGW technique is the wide measuring range [159], the attenuation and dispersion characteristics may cause the long-range propagated UGW signals to be mixed and difficult to interpret [160]. The strand length in the current UGW-based method ranges from 0.9 m to 5.5 m [125, 127, 132, 135], while the length of strands and steel cables in engineering can be tens or even hundreds of meters. Consequently, subsequent studies must focus on the effects of signal attenuation and dispersion of UGW propagating in steel strands or cables over long distances. In the case of the EMI-based method, only localized changes in prestress can be monitored if PZT patches are installed solely on anchor end or on strand surface. Hence, to expand the measuring range of the EMI-based method, it is recommended that multiple PZT patches be attached simultaneously on anchor ends and along the strand length.

3.2. Reliability of Measuring Results. Changes in environmental temperature can directly affect the performance of FBG sensor, ME sensor, and PZT patch, and the UGW signal is also disturbed by temperature change. In addition, environmental disturbances can cause a certain level of noise in monitoring signals. The above factors strongly affect the effectiveness of prestress evaluation results. In terms of the FBG sensor-based method, the temperature compensation FBG sensor is usually installed along with FBG strain sensor [48]. As for the ME sensor-based method, as mentioned in Section 2.2, the improvement of conventional ME sensors [66] or extracting parameters that are insensitive to temperature changes [77] can solve the problem of temperature effects to some extent. Further research can be conducted to further eliminate temperature effect on the performance of ME sensors. For the EMI-based method, current research studies focus on development of temperature compensation algorithms [147–149], and investigation of temperature compensation algorithms with better efficiency can be considered in future studies. Although effects of temperature variation and environmental disturbance on prestress evaluation results based on the UGW-based method have not yet been studied, there is much research progress in damage detection. For example, principal component analysis (PCA) and independent component analysis (ICA) were employed to achieve UGW-based damage assessment of welded steel I-beam under temperature variation [161]; the convolutional neural network (CNN) and UGW were used to classify and localize damage of aluminum plate under the effect of environmental disturbance and temperature variation [162]. Thus, in subsequent studies, the above research achievements can be taken to achieve accurate prestress evaluation under the effects of temperature variation and environmental disturbance. In the case of the electrical resistance-based method, the effect of current thermal effect on prestress measuring results should be concerned.

3.3. Stability and Durability Considering Long-Term Monitoring. Excellent stability and durability are necessary for each method to achieve long-term prestress monitoring. However, no in-depth research has been conducted on this topic. In terms of the FBG-based method, the long-term performance of FBG sensors depends mainly on the encapsulation process [163]. Compared to the surface-attached encapsulation method, the smart strand with embedded FBG sensor undoubtedly has better stability and durability because it effectively avoids breakage due to friction and extrusion between strand and duct [40]. For ME sensors, the influence of friction between sensor and concrete on operating performance needs to be considered if the sensor is embedded inside the concrete; if the ME sensor is utilized for cable force monitoring, the sensor is directly exposed to the external environment, and the sensor performance may be greatly affected due to extreme weather conditions and serious cable vibration. In the case of the EMI-based method

Table 6: Application scenarios, advantages, and limitations for each method.

Method	Application scenario	Advantage	Limitation	Engineering application
FBG sensor-based method	Preinstalled in newly built structures	High precision and high measuring range	Not suitable for in-service structure	Yes
ME sensor-based method	Preinstalled in newly built structures	High precision, high sensitivity, and fast response	Not suitable for in-service structure, vulnerable to temperature	Yes
Dynamic response-based method	Cable structure	High precision, enabling noncontact measurement	Not suitable for embedded steel strand	Yes
UGW-based method	—	Wide detection range and low signal attenuation	The precision acoustoelastic effect-based method is susceptible to measuring errors in the propagation length	No
EMI-based method	—	Sensitive to local damage	Vulnerable to temperature	No
Electrical resistance-based method	—	High sensitivity and small measuring error	Vulnerable to current heating effect	No

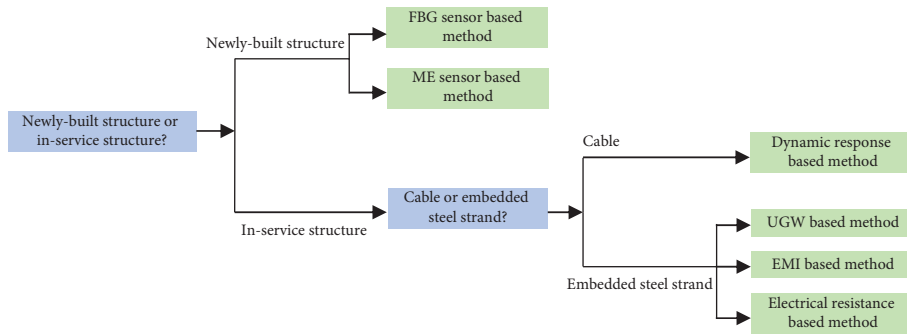

Figure 20: A decision tree for choosing the most appropriate prestress evaluation method in a specific application scenario.

and UGW-based method, the PZT patch is usually attached to the anchor end and the end of steel strand. The bonding performance of PZT determines its service life, and debonding or unreliable bonding of PZT can seriously affect the monitoring results. Therefore, the bonding performance of PZT and structure to be measured should be further investigated. As for the electrical resistance-based method, the process of welding conducting wire to strand end is not suitable for long-term prestress monitoring, as welding point is easy to be broken due to friction. Therefore, it is recommended to carry out further research on reliable approaches to the connection of conductor wire to strand.

3.4. Cost-Efficiency. The high cost of sensor is an important factor limiting its large-scale promotion and application. The time and manpower consumed by sensor installation and maintenance, as well as the time consumed by monitoring data processing, are also factors to be considered. The current costs of FBG sensor and ME sensor and corresponding acquisition devices are still high. Therefore, it is recommended to carry out subsequent research from the perspective of reducing sensor costs. As for the dynamic response-based method, microwave interferometric radar-based [94] and image-based [95, 96, 102] methods do not require cumbersome sensor installation tasks, and the devices are both reusable, which is certainly more valuable for promotion. For the methods based on EMI and UGW, low-cost PZT patches [164, 165] are commonly employed to excite and receive monitoring signals, and the electrical resistance-based method only requires a cheap multimeter to realize data measurements. Thus, the above low-cost methods provide higher promotion value and application prospects. In the UGW technique, extraction of parameters suitable for prestress evaluation from waveform signals is a time-consuming process. It is suggested to carry out research studies on automatic parameter extraction of UGW signals. In addition, wired sensing devices are still utilized in the majority of current prestress evaluation methods, which not only makes the sensor installation cumbersome but also makes the sensor connecting wires easily broken [90]. The wireless sensing systems effectively solve the above problems and have been used in accelerometer [90], FBG sensor [166], and PZT patches [167]. Therefore, the development of the prestress monitoring system with wireless sensing devices is valuable for research.

3.5. Decision Tree-Based Selection for Prestress Assessment Methods. According to the above analysis, there are advantages and certain limitations among various prestress evaluation methods, as shown in Table 6. Therefore, a decision tree is proposed to associate the specific application scenario with the most appropriate prestress evaluation method, as shown in Figure 20. First, we need to judge whether the structure to be tested belongs to the newly built or in-service structure. As for the newly built structure, it is recommended to preinstall FBG sensor or ME sensor in the construction stage to enable real-time prestress monitoring. It is also required to judge whether it belongs to cable or embedded steel strand. In terms of cable structure, the dynamic response-based method is suggested, which is considered to be a mature and high-precision means for cable force monitoring. In terms of embedded steel strand, UGW-based, EMI-based, and electrical resistance-based methods can be considered to be utilized. It is worth noting that the above three methods are only proven to be effective in the laboratory, while the feasibility in practical engineering has yet to be verified.

4. Conclusions

The accurate evaluation of structural effective prestress is of great importance for structural maintenance. The FBG sensor-based, ME sensor-based, dynamic response-based, UGW-based, EMI-based, and electrical resistance-based methods are reviewed in this paper. The principle, application range, and measuring accuracy of each method are introduced and analyzed, and the benefits and limitations of each method are summarized. The main conclusions are as follows:

(1) FBG sensor-based and ME sensor-based methods are widely employed in the monitoring of cable force and embedded strand prestress, and both methods provide high measuring accuracy and have been applied in practical engineering. Constantly improved sensor types, such as smart steel strand with embedded FBG sensor and smart and smart ME sensor, have improved their performance and application range. However, both methods required sensors to be preinstalled in the construction stage and thus not suitable for in-service structures.

(2) Dynamic response-based cable force estimation method provides high measuring accuracy and has already been implemented in engineering, and noncontact measuring is becoming the mainstream of cable vibration monitoring. However, in dynamic response-based prestress estimation for PSC structure, no consensus has been reached on relationship between the variation of prestress and natural frequency, either in theoretical calculations or in experimental experiments.

(3) The main prestress estimation approaches based on the UGW technique include acoustoelastic effect-based, missing frequency band-based, and singular value feature-based approaches. One unavoidable problem in acoustoelastic effect-based approach is that the measuring error in strand length can strongly influence the estimated result, thus resulting in distortion of prestress estimation. The missing frequency band-based and singular value feature-based approaches show higher prediction accuracy and are more suitable for prestress evaluation, although some engineering cases are needed to verify their feasibility and accuracy in the field.

(4) The EMI-based method is effective in prestress monitoring in laboratory experiments, but its field applicability needs to be further verified. As EMI is locally sensitive, the PZT patch may only monitor prestress loss occurring at the anchorage end while may not enable monitoring prestress losses due to concrete shrinkage, creep, and duct friction.

(5) The electrical resistance-based method shows excellent potential for structural prestress evaluation. Since this is only a preliminary study, several factors, such as thermal effect, have not yet been considered. More in-depth studies for this method are needed if engineering applications are to be realized.

(6) As for FBG-based and ME-based methods, development in low-cost sensors and wireless sensing systems is highly recommended. Noncontact vibration measuring approaches are suggested to be promoted in dynamic response-based cable force estimation. For the UGW-based method, it is advisable to carry out research studies on automatic parameter extraction of UGW signal. The temperature sensitivity and temperature compensation algorithm of the EMI technique should be further studied in future research. In the electrical resistance-based method, the factors, such as thermal effect, are suggested to be investigated.

(7) A decision tree is proposed to choose the most appropriate prestress evaluation method in a specific application scenario. As for newly built structure, it is recommended to preinstall FBG sensor or ME sensor in the construction stage to enable real-time prestress monitoring. For in-service cable structure, the dynamic response-based method is suggested. In terms of in-service embedded steel strand, UGW-based, EMI-based, and electrical resistance-based methods can be considered to be utilized. It is worth noting that the above three methods are only proven to be effective in the laboratory, while their feasibility in practical engineering has yet to be verified.

Data Availability

The data can be obtained from the corresponding author upon reasonable request.

Conflicts of Interest

The authors declare that they have no conflicts of interest.

Acknowledgments

The authors are grateful for the financial support received from the National Natural Science Foundation of China (Grant no. 52178449).

References

[1] L. Zhang, Z. Liang, and S. Li, "Effect of current density on the cathodic protection efficiency and mechanical properties of pre-stressed high-strength steel wires for stay cable," *Construction and Building Materials*, vol. 314, Article ID 125671, 2022.

[2] S. Li, L. Zhang, Y. Wang et al., "Effect of cathodic protection current density on corrosion rate of high-strength steel wires for stay cable in simulated dynamic marine atmospheric rainwater," *Structures*, vol. 29, pp. 1655–1670, 2021.

[3] L. Maya and B. Graybeal, "Experimental study of strand splice connections in UHPC for continuous precast prestressed concrete bridges," *Engineering Structures*, vol. 133, pp. 81–90, 2017.

[4] P. Motwani and A. Laskar, "Influence of excessive end slippage on transfer length of prestressing strands in PC members," *Structures*, vol. 20, pp. 676–688, 2019.

[5] M. Elices, A. Valiente, L. Caballero et al., "Failure analysis of prestressed anchor bars," *Engineering Failure Analysis*, vol. 24, pp. 57–66, 2012.

[6] A. Shokoohfar and A. Rahai, "Prediction model of long-term prestress loss interaction for prestressed concrete containment vessels," *Archives of Civil and Mechanical Engineering*, vol. 17, no. 1, pp. 132–144, 2017.

[7] L. J. van der Meer, D. R. W. Martens, and A. T. Vermeltfoort, "Prestress loss due to creep and shrinkage of high-strength calcium silicate element masonry with thin-layer mortar," *Materials and Structures*, vol. 46, no. 12, pp. 2091–2108, 2013.

[8] H. Shi and Q. Guo, "Study of simplified calculating model on friction correlated prestress loss for PC bridges," *IOP Conference Series: Earth and Environmental Science*, vol. 510, no. 5, Article ID 52066, 2020.

[9] P. M. Páez, "Improved prediction of long-term prestress loss in unbonded prestressed concrete members," *Engineering Structures*, vol. 174, pp. 111–125, 2018.

[10] D. Coronelli, C. Mircea, R. Rogers, G. Rosati, and A. N. Consiglio, "Structural assessment of prestressed beams with natural corrosion," *Structural Concrete*, vol. 24, no. 1, pp. 41–55, 2023.

[11] Y. Wang, "Determination of bridge prestress loss under fatigue load based on PSO-BP neural network," *Computational Intelligence and Neuroscience*, vol. 2021, Article ID 4520571, 10 pages, 2021.

[12] H. Zhong and M. Yang, "Prestress loss identification based on dynamic vehicle responses," *Journal of Engineering Mechanics*, vol. 144, no. 9, Article ID 04018088, 2018.

[13] Z. P. Bažant, "Excessive long-time deflections of prestressed box girders. I: record-span bridge in Palau and other paradigms," *Journal of Structural Engineering*, vol. 138, no. 6, pp. 676–686, 2012.

[14] Ministry of Transport of the People's Republic of China, *JTG 3362-2018 Specifications for Design of Highway Reinforced Concrete and Prestress Concrete Bridges and Culverts*, Ministry of Transport of the People's Republic of China, Beijing, China, 1st edition, 2018.

[15] American Concrete Institute, *ACI 318-08 Building Code Requirements for Structural concrete*, American Concrete Institute, Indianapolis, IND, United States, 1st edition, 2014.

[16] American Association of State Highway Officials, *LRFD Bridge Design Specifications*, American Association of State Highway Officials, Washington, DC, USA, 9th edition, 2020.

[17] O. U. Onyemelukwe, P. E. Moussa Issa, and C. J. Mills, "Field measured pre-stress concrete losses versus design code estimates," *Experimental Mechanics*, vol. 43, no. 2, pp. 201–215, 2003.

[18] N. Bagge, J. Nilimaa, and L. Elfgren, "In-situ methods to determine residual prestress forces in concrete bridges," *Engineering Structures*, vol. 135, pp. 41–52, 2017.

[19] M. Bonopera and K.-C. Chang, "Novel method for identifying residual prestress force in simply supported concrete girder-bridges," *Advances in Structural Engineering*, vol. 24, no. 14, pp. 3238–3251, 2021.

[20] A. B. M. Abdullah, J. A. Rice, H. R. Hamilton, and G. R. Consolazio, "An investigation on stressing and breakage response of a prestressing strand using an efficient finite element model," *Engineering Structures*, vol. 123, pp. 213–224, 2016.

[21] T. Lou, S. M. R. Lopes, and A. V. Lopes, "A finite element model to simulate long-term behavior of prestressed concrete girders," *Finite Elements in Analysis and Design*, vol. 81, pp. 48–56, 2014.

[22] Y. El Masri and T. Rakha, "A scoping review of non-destructive testing (NDT) techniques in building performance diagnostic inspections," *Construction and Building Materials*, vol. 265, Article ID 120542, 2020.

[23] A. Joshaghani and D. G. Zollinger, "Concrete pavements curing evaluation with non-destructive tests," *Construction and Building Materials*, vol. 154, pp. 1250–1262, 2017.

[24] L. Séguin-Charbonneau, J. Walter, L.-D. Théroux, L. Scheed, A. Beausoleil, and B. Masson, "Automated defect detection for ultrasonic inspection of CFRP aircraft components," *NDT and E International*, vol. 122, Article ID 102478, 2021.

[25] E. La Malfa Ribolla, M. Rezaee Hajidehi, P. Rizzo, G. Fileccia Scimemi, A. Spada, and G. Giambanco, "Ultrasonic inspection for the detection of debonding in CFRP-reinforced concrete," *Structure and infrastructure engineering*, vol. 14, no. 6, pp. 807–816, 2018.

[26] E. Rossi, R. Polder, O. Copuroglu, T. Nijland, and B. Šavija, "The influence of defects at the steel/concrete interface for chloride-induced pitting corrosion of naturally-deteriorated 20-years-old specimens studied through X-ray Computed Tomography," *Construction and Building Materials*, vol. 235, Article ID 117474, 2020.

[27] M. I. Haith, U. Ewert, and S. Hohendorf, "Radiographic modelling for NDE of subsea pipelines," *NDT and E International*, vol. 86, pp. 113–122, 2017.

[28] K. Tout, A. Meguenani, J.-P. Urban, and C. Cudel, "Automated vision system for magnetic particle inspection of crankshafts using convolutional neural networks," *The International Journal of Advanced Manufacturing Technology*, vol. 112, no. 11-12, pp. 3307–3326, 2021.

[29] N. J. Shipway, P. Huthwaite, M. J. S. Lowe, and T. J. Barden, "Using ResNets to perform automated defect detection for fluorescent penetrant inspection," *NDT and E International*, vol. 119, Article ID 102400, 2021.

[30] N. J. Shipway, T. J. Barden, P. Huthwaite, and M. J. S. Lowe, "Automated defect detection for fluorescent penetrant inspection using random forest," *NDT and E International*, vol. 101, pp. 113–123, 2019.

[31] E. Mohseni, H. Habibzadeh Boukani, D. Ramos França, and M. Viens, "A study of the automated eddy current detection of cracks in steel plates," *Journal of Nondestructive Evaluation*, vol. 39, no. 1, p. 6, 2020.

[32] L. Homa, N. Lorenzo, M. Cherry, and J. Wertz, "Microtexture region segmentation using matching component analysis applied to eddy current testing data," *Journal of Nondestructive Evaluation*, vol. 42, no. 2, p. 39, 2023.

[33] S. Sikdar, W. Ostachowicz, and A. Kundu, "Deep learning for automatic assessment of breathing-debonds in stiffened composite panels using non-linear guided wave signals," *Composite Structures*, vol. 312, Article ID 116876, 2023.

[34] F. Ren, I. N. Giannakeas, Z. Sharif Khodaei, and M. F. Aliabadi, "Sensitivity analysis of temperature effects on guided wave-based damage detection," *Mechanical Systems and Signal Processing*, vol. 196, Article ID 110322, 2023.

[35] S. Zhang, J. Zhou, K. Tan et al., "A prestress testing method for the steel strands inside in-service structures based on the electrical resistance," *Measurement*, vol. 184, Article ID 109930, 2021.

[36] B. Heitner, E. J. Obrien, T. Yalamas, and F. Schoefs, "Updating probabilities of bridge reinforcement corrosion using health monitoring data," *Engineering Structures*, vol. 190, pp. 41–51, 2019.

[37] M. Furinghetti, A. Pavese, F. Lunghi, and D. Silvestri, "Strategies of structural health monitoring for bridges based on cloud computing," *Journal of Civil Structural Health Monitoring*, vol. 9, no. 5, pp. 607–616, 2019.

[38] D. Cao, X. Qin, S. Meng, Y. Tu, L. Elfgren, and N. Sabourova, "Evaluation of prestress losses in prestressed concrete specimens subjected to freeze–thaw cycles," *Structure and infrastructure engineering*, vol. 12, no. 2, pp. 159–170, 2016.

[39] L. A. Caro, J. R. Martí-Vargas, and P. Serna, "Prestress losses evaluation in prestressed concrete prismatic specimens," *Engineering Structures*, vol. 48, pp. 704–715, 2013.

[40] W. Zhu, Q. Shen, and H. Qin, "Monitoring of prestress and bond stress of self-sensing FBG steel strand," *Measurement*, vol. 177, Article ID 109246, 2021.

[41] S. Zhang, J. Zhou, H. Zhang, L. Liao, and L. Liu, "Influence of cable tension history on the monitoring of cable tension using magnetoelastic inductance method," *Structural Health Monitoring*, vol. 20, no. 6, pp. 3392–3405, 2021.

[42] K.-D. Nguyen and J.-T. Kim, "Smart PZT-interface for wireless impedance-based prestress-loss monitoring in tendon-anchorage connection," *Smart Structures and Systems*, vol. 9, no. 6, pp. 489–504, 2012.

[43] J.-T. Kim, J.-H. Park, D. S. Hong, and W.-S. Park, "Hybrid health monitoring of prestressed concrete girder bridges by

sequential vibration-impedance approaches," *Engineering Structures*, vol. 32, no. 1, pp. 115–128, 2010.

[44] J. M. Kim, H.-W. Kim, S.-Y. Choi, and S.-Y. Park, "Measurement of prestressing force in pretensioned UHPC deck using a fiber optic FBG sensor embedded in a 7-wire strand," *Journal of Sensors*, vol. 2016, Article ID 8634080, 9 pages, 2016.

[45] P. M. Nellen, "Strain measurements on concrete beam and carbon fiber cable with distributed optical fiber Bragg grating sensors," *Optical Engineering*, vol. 35, p. 2570, 1996.

[46] Z. Zhou, J. He, G. Chen, and J. Ou, "A smart steel strand for the evaluation of prestress loss distribution in post-tensioned concrete structures," *Journal of Intelligent Material Systems and Structures*, vol. 20, no. 16, pp. 1901–1912, 2009.

[47] D. Li, Z. Zhou, and J. Ou, "Development and sensing properties study of FRP-FBG smart stay cable for bridge health monitoring applications," *Measurement*, vol. 44, no. 4, pp. 722–729, 2011.

[48] D. Li, Z. Zhou, and J. Ou, "Dynamic behavior monitoring and damage evaluation for arch bridge suspender using GFRP optical fiber Bragg grating sensors," *Optics and Laser Technology*, vol. 44, no. 4, pp. 1031–1038, 2012.

[49] J.-M. Kim, H.-W. Kim, Y. H. Park, and I. H. Yang, "FBG sensors encapsulated into 7-wire steel strand for tension monitoring of a prestressing tendon," *Advances in Structural Engineering*, vol. 15, no. 6, pp. 907–917, 2012.

[50] J. He, Z. Zhou, and O. Jinping, "Optic fiber sensor-based smart bridge cable with functionality of self-sensing," *Mechanical Systems and Signal Processing*, vol. 35, no. 1-2, pp. 84–94, 2013.

[51] C. Lan, Z. Zhou, and J. Ou, "Monitoring of structural prestress loss in RC beams by inner distributed Brillouin and fiber Bragg grating sensors on a single optical fiber," *Structural Control and Health Monitoring*, vol. 21, no. 3, pp. 317–330, 2014.

[52] S. Li and M. Zhou, "Long-term mechanical properties of smart cable based on FBG desensitized encapsulation sensors," *Photonic Sensors*, vol. 4, no. 3, pp. 236–241, 2014.

[53] S. Kim, Y. H. Park, S. Park, K. Cho, and J.-R. Cho, "A sensor-type PC strand with an embedded FBG sensor for monitoring prestress forces," *Sensors*, vol. 15, no. 1, pp. 1060–1070, 2015.

[54] T. C. Huynh and J.-T. Kim, "FOS-based prestress force monitoring and temperature effect estimation in unbonded tendons of PSC girders," *Journal of Aerospace Engineering*, vol. 30, no. 2, Article ID B4016005, 2017.

[55] J.-M. Kim, C.-M. Kim, S.-Y. Choi, and B. Y. Lee, "Enhanced strain measurement range of an FBG sensor embedded in seven-wire steel strands," *Sensors*, vol. 17, no. 7, p. 1654, 2017.

[56] R. Zheng, L. Liu, X. Zhao, Z. Chen, C. Zhang, and X. Hua, "Investigation of measurability and reliability of adhesive-bonded built-in fiber Bragg grating sensors on steel wire for bridge cable force monitoring," *Measurement*, vol. 129, pp. 349–357, 2018.

[57] D. Dan, P. Jia, G. Li, and P. Niu, "Experimental study on mechanical and sensing properties of smart composite prestressed tendon," *Materials*, vol. 11, p. 2087, 2018.

[58] T. Jiao, Z. Zhou, J. Liu, H. Xiao, and J. Ou, "Large strain-tolerated smart steel strand with built in coaxial cable Fabry–Perot interferometer," *Measurement*, vol. 151, Article ID 107019, 2020.

[59] P. Biswas, S. Bandyopadhyay, K. Kesavan et al., "Investigation on packages of fiber Bragg grating for use as embeddable strain sensor in concrete structure," *Sensors and Actuators A: Physical*, vol. 157, no. 1, pp. 77–83, 2010.

[60] Ministry of Transport of the People's Republic of China, *JTG/T D65-01-2007 Guidelines for Design of Highway cable-stayed Bridge*, Ministry of Transport of the People's Republic of China, Beijing, China, 1st edition, 2007.

[61] Ministry of Transport of the People's Republic of China, *JTG/T D65-05-2015 Specifications for Design of Highway Suppension Bridge*, Ministry of Transport of the People's Republic of China, Beijing, China, 1st edition, 2015.

[62] B. Özkale, N. Shamsudhin, T. Bugmann, B. J. Nelson, and S. Pané, "Magnetostriction in electroplated CoFe alloys," *Electrochemistry Communications*, vol. 76, pp. 15–19, 2017.

[63] T. A. Baudendistel and M. L. Turner, "A novel inverse-magnetostrictive force sensor," *IEEE Sensors Journal*, vol. 7, no. 2, pp. 245–250, 2007.

[64] S. Zhang, J. Zhou, Y. Zhou, H. Zhang, and J. Chen, "Cable tension monitoring based on the elasto-magnetic effect and the self-induction phenomenon," *Materials*, vol. 12, no. 14, p. 2230, 2019.

[65] S. Sumitro, S. Kurokawa, K. Shimano, and M. L. Wang, "Monitoring based maintenance utilizing actual stress sensory technology," *Smart Materials and Structures*, vol. 14, no. 3, pp. 68–78, 2005.

[66] D. Tang, S. Huang, W. Chen, and J. Jiang, "Study of a steel strand tension sensor with difference single bypass excitation structure based on the magneto-elastic effect," *Smart Materials and Structures*, vol. 17, no. 2, Article ID 25019, 2008.

[67] C. Joh, J. W. Lee, and I. Kwahk, "Feasibility study of stress measurement in prestressing tendons using villari effect and induced magnetic field," *International Journal of Distributed Sensor Networks*, vol. 9, no. 11, Article ID 249829, 2013.

[68] R. Zhang, Y. Duan, S. Or, and Y. Zhao, "Smart elasto-magneto-electric (EME) sensors for stress monitoring of steel cables: design theory and experimental validation," *Sensors*, vol. 14, no. 8, pp. 13644–13660, 2014.

[69] D. Tang, H. Zhu, J. Mou, and M. Wu, "Research on the temperature influence and compensation technique in a magneto-elastic cable tension sensor," *International Journal of Sensor Networks*, vol. 16, no. 4, pp. 236–243, 2014.

[70] K. Cho, J.-R. Cho, S. Kim, S. Park, Y.-J. Kim, and Y.-H. Park, "Estimation of prestress force distribution in multi-strand system of prestressed concrete structures using field data measured by electromagnetic sensor," *Sensors*, vol. 16, no. 8, p. 1317, 2016.

[71] Y. Duan, R. Zhang, C. Dong et al., "Development of elasto-magneto-electric (EME) sensor for in-service cable force monitoring," *International Journal of Structural Stability and Dynamics*, vol. 16, no. 4, Article ID 1640016, 2016.

[72] C. Xiu, L. Ren, H. Li, and Z. Jia, "Study on an innovative self-inductance tension eddy current sensor based on the inverse magnetostrictive effect," *Sensor Review*, vol. 37, no. 1, pp. 43–53, 2017.

[73] L. Ren, C. Xiu, H. Li, Y. Lu, J. Wang, and X. Yao, "Development of elasto-magnetic (EM) sensor for monitoring cable tension using an innovative ratio measurement method," *Smart Materials and Structures*, vol. 27, no. 11, Article ID 115003, 2018.

[74] R. Zhang, Y. Duan, Y. Zhao, and X. He, "Temperature compensation of elasto-magneto-electric (EME) sensors in cable force monitoring using BP neural network," *Sensors*, vol. 18, no. 7, p. 2176, 2018.

[75] Z. Chen and S. Zhang, "EM-based monitoring and probabilistic analysis of prestress loss of bonded tendons in PSC

beams," *Advances in Civil Engineering*, vol. 2018, Article ID 4064362, 9 pages, 2018.

[76] X. Liu, D. Wu, C. He, H. Feng, and B. Wu, "Comparison of AC and pulsed magnetization-based elasto-magnetic methods for tensile force measurement in steel strand," *Measurement*, vol. 117, pp. 410–418, 2018.

[77] H. Feng, X. Liu, B. Wu, D. Wu, X. Zhang, and C. He, "Temperature-insensitive cable tension monitoring during the construction of a cable-stayed bridge with a custom-developed pulse elasto-magnetic instrument," *Structural Health Monitoring*, vol. 18, no. 5-6, pp. 1982–1994, 2018.

[78] T. Guo, Z. Chen, S. Lu, and R. Yao, "Monitoring and analysis of long-term prestress losses in post-tensioned concrete beams," *Measurement*, vol. 122, pp. 573–581, 2018.

[79] J. Kim and S. Park, "Field applicability of a machine learning–based tensile force estimation for pre-stressed concrete bridges using an embedded elasto-magnetic sensor," *Structural Health Monitoring*, vol. 19, no. 1, pp. 281–292, 2020.

[80] Z. Liu, S. Liu, C. Xie, and G. Bai, "Non-invasive force measurement based on magneto-elastic effect for steel wire ropes," *IEEE Sensors Journal*, vol. 21, no. 7, pp. 8979–8987, 2021.

[81] S. Zhang, H. Zhang, H. Liu, J. Zhou, C. Yin, and L. Liao, "Resonance enhanced magnetoelastic method with high sensitivity for steel stress measurement," *Measurement*, vol. 186, Article ID 110139, 2021.

[82] A. Meixedo, J. Santos, D. Ribeiro, R. Calçada, and M. Todd, "Damage detection in railway bridges using traffic-induced dynamic responses," *Engineering Structures*, vol. 238, Article ID 112189, 2021.

[83] H. Khodabandehlou, G. Pekcan, and M. S. Fadali, "Vibration-based structural condition assessment using convolution neural networks," *Structural Control and Health Monitoring*, Article ID e2308, 2018.

[84] C.-P. Yu, "Tension prediction for straight cables based on effective vibration length with a two-frequency approach," *Engineering Structures*, vol. 222, Article ID 111121, 2020.

[85] Y. Bao, Z. Shi, J. L. Beck, H. Li, and T. Y. Hou, "Identification of time-varying cable tension forces based on adaptive sparse time-frequency analysis of cable vibrations," *Structural Control and Health Monitoring*, vol. 24, no. 3, Article ID e1889, 2017.

[86] Z. Fu, B. Ji, Q. Wang, and Y. Wang, "Cable force calculation using vibration frequency methods based on cable geometric parameters," *Journal of Performance of Constructed Facilities*, vol. 31, no. 4, Article ID 04017021, 2017.

[87] B. H. Kim and T. Park, "Estimation of cable tension force using the frequency-based system identification method," *Journal of Sound and Vibration*, vol. 304, no. 3-5, pp. 660–676, 2007.

[88] S. Cho, J. P. Lynch, J. J. Lee, and C.-B. Yun, "Development of an automated wireless tension force estimation system for cable-stayed bridges," *Journal of Intelligent Material Systems and Structures*, vol. 21, no. 3, pp. 361–376, 2010.

[89] D.-H. Choi and W.-S. Park, "Tension force estimation of extradosed bridge cables oscillating nonlinearly under gravity effects," *International Journal of Steel Structures*, vol. 11, no. 3, pp. 383–394, 2011.

[90] Y. Yu, C. Zhang, X. Zhu, W. H. Kang, X. Mao, and B. Uy, "Design and experimental investigations of a vibration based wireless measurement system for bridge cable tension monitoring," *Advances in Structural Engineering*, vol. 17, no. 11, pp. 1657–1668, 2014.

[91] X. Zhao, R. Han, Y. Ding et al., "Portable and convenient cable force measurement using smartphone," *Journal of Civil Structural Health Monitoring*, vol. 5, no. 4, pp. 481–491, 2015.

[92] B. J. Rango, F. J. Serralunga, M. T. Piovan, J. S. Ballaben, and M. B. Rosales, "Identification of the tension force in cables with insulators," *Meccanica*, vol. 54, no. 1-2, pp. 33–46, 2019.

[93] B. Yan, W. Chen, J. Yu, and X. Jiang, "Mode shape-aided tension force estimation of cable with arbitrary boundary conditions," *Journal of Sound and Vibration*, vol. 440, pp. 315–331, 2019.

[94] W. Zhao, G. Zhang, and J. Zhang, "Cable force estimation of a long-span cable-stayed bridge with microwave interferometric radar," *Computer-Aided Civil and Infrastructure Engineering*, vol. 35, no. 12, pp. 1419–1433, 2020.

[95] S. W. Kim, J. Cheung, J. Park, and S. Na, "Image-based back analysis for tension estimation of suspension bridge hanger cables," *Structural Control and Health Monitoring*, vol. 27, no. 4, Article ID e2508, 2020.

[96] W. Du, D. Lei, P. Bai, F. Zhu, and Z. Huang, "Dynamic measurement of stay-cable force using digital image techniques," *Measurement*, vol. 151, Article ID 107211, 2020.

[97] B. Yan, D. Li, W. Chen, L. Deng, and X. Jiang, "Mode shape–aided cable force determination using digital image correlation," *Structural Health Monitoring*, vol. 20, no. 5, pp. 2430–2445, 2021.

[98] C. Chu, F. Ghrib, and S. Cheng, "Cable tension monitoring through feature-based video image processing," *Journal of Civil Structural Health Monitoring*, vol. 11, no. 1, pp. 69–84, 2021.

[99] S. Jeong, H. Kim, J. Lee, and S.-H. Sim, "Automated wireless monitoring system for cable tension forces using deep learning," *Structural Health Monitoring*, vol. 20, no. 4, pp. 1805–1821, 2021.

[100] D. Jana and S. Nagarajaiah, "Computer vision-based real-time cable tension estimation in Dubrovnik cable-stayed bridge using moving handheld video camera," *Structural Control and Health Monitoring*, vol. 28, no. 5, Article ID e2713, 2021.

[101] H. C. Jo, S. H. Kim, J. Lee, H.-G. Sohn, and Y. M. Lim, "Sag-based cable tension force evaluation of cable-stayed bridges using multiple digital images," *Measurement*, vol. 186, Article ID 110053, 2021.

[102] Y. Tian, C. Zhang, S. Jiang, J. Zhang, and W. Duan, "Noncontact cable force estimation with unmanned aerial vehicle and computer vision," *Computer-Aided Civil and Infrastructure Engineering*, vol. 36, no. 1, pp. 73–88, 2021.

[103] Y. Wang, K. Li, Y. Chen, S. Xu, and W. Shou, "Research on non-contact and non-fixed cable force measurement based on smartphone," *Applied Sciences*, vol. 11, no. 19, p. 8902, 2021.

[104] Z. Yu, S. Shao, N. Liu et al., "Cable tension identification based on near field radiated acoustic pressure signal," *Measurement*, vol. 178, Article ID 109354, 2021.

[105] C. Zhang, Y. Tian, and J. Zhang, "Complex image background segmentation for cable force estimation of urban bridges with drone-captured video and deep learning," *Structural Control and Health Monitoring*, vol. 29, no. 4, Article ID e2910, 2022.

[106] D. Jana, S. Nagarajaiah, Y. Yang, and S. Li, "Real-time cable tension estimation from acceleration measurements using wireless sensors with packet data losses: analytics with compressive sensing and sparse component analysis," *Journal of Civil Structural Health Monitoring*, vol. 12, no. 4, pp. 797–815, 2022.

[107] S. Wangchuk, D. M. Siringoringo, and Y. Fujino, "Modal analysis and tension estimation of stay cables using non-contact vision-based motion magnification method," *Structural Control and Health Monitoring*, vol. 29, no. 7, 2022.

[108] D. Jana, S. Nagarajaiah, and Y. Yang, "Computer vision-based real-time cable tension estimation algorithm using complexity pursuit from video and its application in Fred-Hartman cable-stayed bridge," *Structural Control and Health Monitoring*, vol. 29, no. 9, 2022.

[109] S.-W. Kim, D.-U. Park, J.-S. Kim, and J.-B. Park, "Estimating tension of a prestressed concrete cable-stayed bridge under construction and traffic use conditions using a vision-based system," *Structures*, vol. 47, pp. 299–312, 2023.

[110] W. Wang, D. Cui, C. Ai et al., "Target-free recognition of cable vibration in complex backgrounds based on computer vision," *Mechanical Systems and Signal Processing*, vol. 197, Article ID 110392, 2023.

[111] M. Saiidi, B. Douglas, and S. Feng, "Prestress force effect on vibration frequency of concrete bridges," *Journal of Structural Engineering*, vol. 120, no. 7, pp. 2233–2241, 1994.

[112] D.-D. Ho, J.-T. Kim, N. Stubbs, and W.-S. Park, "Prestress-force estimation in PSC girder using modal parameters and system identification," *Advances in Structural Engineering*, vol. 15, no. 6, pp. 997–1012, 2012.

[113] T. Hop, "The effect of degree of prestressing and age of concrete beams on frequency and damping of their free vibration," *Materials and Structures*, vol. 24, no. 3, pp. 210–220, 1991.

[114] B. H. Kim, J. B. Jang, H. P. Lee, and D. H. Lee, "Effect of prestress force on longitudinal vibration of bonded tendons embedded in a nuclear containment," *Nuclear Engineering and Design*, vol. 240, no. 6, pp. 1281–1289, 2010.

[115] X. Zhong, T. Yang, M. Shen, J. Yu, and X. Xie, "Method for testing the tension of vertical prestressing bars in webs of concrete box girder bridges," *Journal of Bridge Engineering*, vol. 16, no. 3, pp. 438–444, 2011.

[116] D. Noble, M. Nogal, A. O'Connor, and V. Pakrashi, "The effect of prestress force magnitude and eccentricity on the natural bending frequencies of uncracked prestressed concrete beams," *Journal of Sound and Vibration*, vol. 365, pp. 22–44, 2016.

[117] R. Rashetnia, F. Ghasemzadeh, M. Hallaji, and M. Pour-Ghaz, "Quantifying prestressing force loss due to corrosion from dynamic structural response," *Journal of Sound and Vibration*, vol. 433, pp. 129–137, 2018.

[118] M. Bonopera, K. C. Chang, C. C. Chen, Y. C. Sung, and N. Tullini, "Experimental study on the fundamental frequency of prestressed concrete bridge beams with parabolic unbonded tendons," *Journal of Sound and Vibration*, vol. 455, pp. 150–160, 2019.

[119] E. Hamed and Y. Frostig, "Natural frequencies of bonded and unbonded prestressed beams–prestress force effects," *Journal of Sound and Vibration*, vol. 295, no. 1-2, pp. 28–39, 2006.

[120] B.-Z. Gan, S.-P. Chiew, Y. Lu, and T.-C. Fung, "The effect of prestressing force on natural frequencies of concrete beams-A numerical validation of existing experiments by modelling shrinkage crack closure," *Journal of Sound and Vibration*, vol. 455, pp. 20–31, 2019.

[121] P. W. Loveday, "Guided wave inspection and monitoring of railway track," *Journal of Nondestructive Evaluation*, vol. 31, no. 4, pp. 303–309, 2012.

[122] B. Zhong, J. Zhu, and G. Morcous, "Measuring acoustoelastic coefficients for stress evaluation in concrete," *Construction and Building Materials*, vol. 309, Article ID 125127, 2021.

[123] P. Nazarko and L. Ziemiański, "Application of elastic waves and neural networks for the prediction of forces in bolts of flange connections subjected to static tension tests," *Materials*, vol. 13, no. 16, p. 3607, 2020.

[124] M. Rucka, "Monitoring steel bolted joints during a monotonic tensile test using linear and nonlinear lamb wave methods: a feasibility study," *Metals*, vol. 8, no. 9, p. 683, 2018.

[125] B. Dubuc, A. Ebrahimkhanlou, and S. Salamone, "Higher order longitudinal guided wave modes in axially stressed seven-wire strands," *Ultrasonics*, vol. 84, pp. 382–391, 2018.

[126] F. Treyssède, A. Frikha, and P. Cartraud, "Mechanical modeling of helical structures accounting for translational invariance. Part 2: guided wave propagation under axial loads," *International Journal of Solids and Structures*, vol. 50, no. 9, pp. 1383–1393, 2013.

[127] Q. Ji, L. Jian-Bin, L. Fan-Rui, Z. Jian-Ting, and W. Xu, "Stress evaluation in seven-wire strands based on singular value feature of ultrasonic guided waves," *Structural Health Monitoring*, vol. 21, no. 2, pp. 518–533, 2022.

[128] Z. Abbasi and F. Honarvar, "Evaluation of the sensitivity of higher order modes cluster (HOMC) guided waves to plate defects," *Applied Acoustics*, vol. 187, Article ID 108512, 2022.

[129] Z. Abbasi and D. Ozevin, "Acoustoelastic coefficients in thick steel plates under normal and shear stresses," *Experimental Mechanics*, vol. 56, no. 9, pp. 1559–1575, 2016.

[130] C. M. Kube and A. N. Norris, "Stress formulation of acoustoelasticity," *Wave Motion*, vol. 114, Article ID 103002, 2022.

[131] S. Chaki and G. Bourse, "Stress level measurement in prestressed steel strands using acoustoelastic effect," *Experimental Mechanics*, vol. 49, no. 5, pp. 673–681, 2009.

[132] S. Chaki and G. Bourse, "Guided ultrasonic waves for non-destructive monitoring of the stress levels in prestressed steel strands," *Ultrasonics*, vol. 49, no. 2, pp. 162–171, 2009.

[133] H. Kwun, K. A. Bartels, and J. J. Hanley, "Effects of tensile loading on the properties of elastic-wave propagation in a strand," *Journal of the Acoustical Society of America*, vol. 103, no. 6, pp. 3370–3375, 1998.

[134] F. Treyssède, "Dispersion curve veering of longitudinal guided waves propagating inside prestressed seven-wire strands," *Journal of Sound and Vibration*, vol. 367, pp. 56–68, 2016.

[135] X. Liu, B. Wu, F. Qin, C. He, and Q. Han, "Observation of ultrasonic guided wave propagation behaviours in pre-stressed multi-wire structures," *Ultrasonics*, vol. 73, pp. 196–205, 2017.

[136] M. Tang, X. Wu, M. Cong, and K. Guo, "A method based on SVD for detecting the defect using the magnetostrictive guided wave technique," *Mechanical Systems and Signal Processing*, vol. 70-71, pp. 601–612, 2016.

[137] P. W. Loveday, C. S. Long, and D. A. Ramatlo, "Ultrasonic guided wave monitoring of an operational rail track," *Structural Health Monitoring*, vol. 19, no. 6, pp. 1666–1684, 2020.

[138] D. Ai, H. Luo, and H. Zhu, "Numerical and experimental investigation of flexural performance on pre-stressed concrete structures using electromechanical admittance," *Mechanical Systems and Signal Processing*, vol. 128, pp. 244–265, 2019.

[139] P. Negi, T. Chakraborty, and S. Bhalla, "Viability of electro-mechanical impedance technique for monitoring damage in rocks under cyclic loading," *Acta Geotechnica*, vol. 17, no. 2, pp. 483–495, 2022.

[140] T. Bansal, V. Talakokula, and K. Mathiyazhagan, "Equivalent structural parameters based non-destructive prediction of sustainable concrete strength using machine learning models via piezo sensor," *Measurement*, vol. 187, Article ID 110202, 2022.

[141] T. Bansal, V. Talakokula, and P. Sathujoda, "Durability aspects of blended concrete systems subjected to combined mechanical and environmental loading using piezo sensor," *Construction and Building Materials*, vol. 348, Article ID 128613, 2022.

[142] D. de Souza Rabelo, J. D. Hobeck, D. J. Inman, R. M. Finzi Neto, and V. Steffen, "Real-time structural health monitoring of fatigue crack on aluminum beam using an impedance-based portable device," *Journal of Intelligent Material Systems and Structures*, vol. 28, no. 20, pp. 3152–3162, 2017.

[143] P. H. Malinowski, T. Wandowski, and S. K. Singh, "Employing principal component analysis for assessment of damage in GFRP composites using electromechanical impedance," *Composite Structures*, vol. 266, Article ID 113820, 2021.

[144] T. Morwal, T. Bansal, A. Azam, and V. Talakokula, "Monitoring chloride-induced corrosion in metallic and reinforced/prestressed concrete structures using piezo sensors-based electro-mechanical impedance technique: a review," *Measurement*, vol. 218, Article ID 113102, 2023.

[145] T. Bansal and V. Talakokula, "Deterioration of structural parameters due to corrosion in prestressed concrete identified by smart probe-based piezo sensor," *Engineering Research Express*, vol. 3, no. 1, Article ID 15011, 2021.

[146] T. Huynh and J.-T. Kim, "Quantitative damage identification in tendon anchorage via PZT interface- based impedance monitoring technique," *Smart Structures and Systems*, vol. 20, pp. 181–195, 2017.

[147] T. C. Huynh and J.-T. Kim, "Quantification of temperature effect on impedance monitoring via PZT interface for prestressed tendon anchorage," *Smart Materials and Structures*, vol. 26, no. 12, Article ID 125004, 2017.

[148] T. Huynh, N.-L. Dang, and J.-T. Kim, "PCA-based filtering of temperature effect on impedance monitoring in prestressed tendon anchorage," *Smart Structures and Systems*, vol. 22, pp. 57–70, 2018.

[149] T. C. Huynh and J.-T. Kim, "RBFN-based temperature compensation method for impedance monitoring in prestressed tendon anchorage," *Structural Control and Health Monitoring*, vol. 25, no. 6, Article ID e2173, 2018.

[150] J.-Y. Ryu, T. C. Huynh, and J.-T. Kim, "Tension force estimation in axially loaded members using wearable piezoelectric interface technique," *Sensors*, vol. 19, no. 1, p. 47, 2018.

[151] N. Dang, T. Huynh, and Q. Pham, "Damage-sensitive impedance sensor placement on multi-strand anchorage based on local stress variation analysis," *Structural Control and Health Monitoring*, vol. 27, no. 7, Article ID e2547, 2020.

[152] N. L. Dang, Q. Q. Pham, and J. T. Kim, "Piezoelectric-based hoop-type interface for impedance monitoring of local strand breakage in prestressed multi-strand anchorage," *Structural Control and Health Monitoring*, vol. 28, no. 1, Article ID e2649, 2021.

[153] T.-C. Le, T. T. V. Phan, T.-H. Nguyen, D.-D. Ho, and T. C. Huynh, "A low-cost prestress monitoring method for post-tensioned RC beam using piezoelectric-based smart strand," *Buildings*, vol. 11, no. 10, p. 431, 2021.

[154] L. Liu, Y. Xu, Z. Wang, G. Li, X. Wang, and Y. Huang, "Probing and separating corrosion and erosion of pipeline steel using electrical resistance method in conjunction with electrochemical measurements," *Measurement*, vol. 183, Article ID 109797, 2021.

[155] W. Dong, Y. Huang, B. Lehane, and G. Ma, "XGBoost algorithm-based prediction of concrete electrical resistivity for structural health monitoring," *Automation in Construction*, vol. 114, Article ID 103155, 2020.

[156] S. H. Ghasemzadeh Mosavinejad, J. Barandoust, A. Ghanizadeh, and M. Sigari, "Crack detection of a HPCFRCC thin plate using electrical resistivity method," *Construction and Building Materials*, vol. 193, pp. 255–267, 2018.

[157] N. Alshwawreh, B. Alhamarneh, Q. Altwarah, S. Quandour, S. Barghout, and O. Ayasrah, "Electrical resistivity and tensile strength relationship in heat-treated all aluminum alloy wire conductors," *Materials*, vol. 14, no. 19, p. 5738, 2021.

[158] T. Sasaki, J. Park, K. Soga et al., "Distributed fibre optic strain sensing of an axially deformed well model in the laboratory," *Journal of Natural Gas Science and Engineering*, vol. 72, Article ID 103028, 2019.

[159] B. Dubuc, A. Ebrahimkhanlou, and S. Salamone, "Stress monitoring of prestressing strands in corrosive environments using modulated higher-order guided ultrasonic waves," *Structural Health Monitoring*, vol. 19, no. 1, pp. 202–214, 2020.

[160] M. Legg and M. K. Yücel, "Increased range of ultrasonic guided wave testing of overhead transmission line cables using dispersion compensation," *Ultrasonics*, vol. 62, pp. 35–45, 2015.

[161] J. Tu, Z. Tang, C. Yun, J. Wu, and X. Xu, "Guided wave-based damage assessment on welded steel I-beam under ambient temperature variations," *Structural Control and Health Monitoring*, vol. 28, no. 4, Article ID e2696, 2021.

[162] S. Sawant, S. Patil, J. Thalapil, S. Banerjee, and S. Tallur, "Temperature variation compensated damage classification and localisation in ultrasonic guided wave SHM using self-learnt features and Gaussian mixture models," *Smart Materials and Structures*, vol. 31, no. 5, Article ID 55008, 2022.

[163] J. de Pelegrin, U. J. Dreyer, K. M. Sousa, and J. C. Cardozo da Silva, "Smart carbon-fiber reinforced polymer optical fiber Bragg grating for monitoring fault detection in bearing," *IEEE Sensors Journal*, vol. 22, no. 13, pp. 12921–12929, 2022.

[164] P. Junior, D. M. D'Addona, and P. R. Aguiar, "Dressing tool condition monitoring through impedance-based sensors: Part 1-PZT diaphragm transducer response and EMI sensing technique," *Sensors*, vol. 18, no. 12, p. 4455, 2018.

[165] Y. Bhuiyan, B. Lin, and V. Giurgiutiu, "Characterization of piezoelectric wafer active sensor for acoustic emission sensing," *Ultrasonics*, vol. 92, pp. 35–49, 2019.

[166] T. Ezzedine and A. Zrelli, "Efficient measurement of temperature, humidity and strain variation by modeling reflection Bragg grating spectrum in WSN," *Optik*, vol. 135, pp. 454–462, 2017.

[167] H. Fu, Z. Sharif-Khodaei, and M. F. Aliabadi, "An energy-efficient cyber-physical system for wireless on-board aircraft structural health monitoring," *Mechanical Systems and Signal Processing*, vol. 128, pp. 352–368, 2019.